LETTER

Gamma oscillations organize top–down signalling to hypothalamus and enable food seeking

Marta Carus-Cadavieco[1]*, Maria Gorbati[1]*, Li Ye[2,3], Franziska Bender[1], Suzanne van der Veldt[1], Christin Kosse[4], Christoph Börgers[5], Soo Yeun Lee[2], Charu Ramakrishnan[2], Yubin Hu[1], Natalia Denisova[1], Franziska Ramm[1], Emmanouela Volitaki[1], Denis Burdakov[4], Karl Deisseroth[2,3,6], Alexey Ponomarenko[1]* & Tatiana Korotkova[1]*

Both humans and animals seek primary rewards in the environment, even when such rewards do not correspond to current physiological needs. An example of this is a dissociation between food-seeking behaviour and metabolic needs, a notoriously difficult-to-treat symptom of eating disorders. Feeding relies on distinct cell groups in the hypothalamus[1–4], the activity of which also changes in anticipation of feeding onset[5–7]. The hypothalamus receives strong descending inputs from the lateral septum, which is connected, in turn, with cortical networks[8], but cognitive regulation of feeding-related behaviours is not yet understood. Cortical cognitive processing[9,10] involves gamma oscillations[11–15], which support memory[16,17], attention[18], cognitive flexibility[19] and sensory responses[20]. These functions contribute crucially to feeding behaviour by unknown neural mechanisms. Here we show that coordinated gamma (30–90 Hz) oscillations in the lateral hypothalamus and upstream brain regions organize food-seeking behaviour in mice. Gamma-rhythmic input to the lateral hypothalamus from somatostatin-positive lateral septum cells evokes food approach without affecting food intake. Inhibitory inputs from the lateral septum enable separate signalling by lateral hypothalamus neurons according to their feeding-related activity, making them fire at distinct phases of the gamma oscillation. Upstream, medial prefrontal cortical projections provide gamma-rhythmic inputs to the lateral septum; these inputs are causally associated with improved performance in a food-rewarded learning task. Overall, our work identifies a top–down pathway that uses gamma synchronization to guide the activity of subcortical networks and to regulate feeding behaviour by dynamic reorganization of functional cell groups in the hypothalamus.

Top-down forebrain innervation of the lateral hypothalamus (LH) is provided, to a large extent, by inhibitory inputs from the lateral septum (LS)[8], a key region for governing innate behaviours according to environmental context[21–23]. To investigate coordination between the LS and LH, we recorded neuronal firing and local field potential (LFP) from the LH and LS in mice during spontaneous behaviour in the free-access feeding model (Fig. 1a, b, Extended Data Fig. 1a–g). LFP in the LS and LH displayed prominent gamma oscillations (30–90 Hz; Fig. 1b, Extended Data Fig. 1h, i), which entrained neuronal activity within and across the two regions (Fig. 1c, d) and synchronized large neuronal populations (Extended Data Fig. 1j, Fig. 1e). When mice were approaching the food zone, the power of gamma oscillations in the LS and LH matched the time required to reach the food zone (Fig. 1f, Extended Data Fig. 1k and Supplementary Information, Statistical Analysis), but not the drinking zone (Extended Data Fig. 1l and Supplementary Information, Statistical Analysis).

To address whether LS–LH gamma synchronization causally influences food-seeking behaviour, we targeted the engineered channel-rhodopsin-2 (ChR2) variant ChETA to LS GABA (γ-aminobutyric acid) cells in Vgat-Cre mice, or to the population of somatostatin-expressing LS GABA neurons projecting to the LH (LS$_{SST}$) in Sst-Cre mice (Allen Mouse Brain Atlas; Fig. 1g, Extended Data Fig. 2a–c). Optogenetic gamma-frequency stimulation of LS projections efficiently entrained most (72.5%) LH neurons and evoked gamma oscillations in the LH (Fig. 1g). Gamma-frequency stimulation of LS$_{SST}$–LH projections facilitated food-seeking behaviour, that is, shortened the latency to reach the food zone (Fig. 1h, Extended Data Fig. 2e), but not a control zone (Fig. 1i) or the drinking zone (Extended Data Fig. 2d); it also did not change the average running speed (Extended Data Fig. 2f and Supplementary Information, Statistical Analysis). Gamma-frequency stimulation also increased the probability of entering the food zone before food-free zones, located in other corners of the enclosure (Fig. 1j), whereas stimulation at a non-gamma frequency (9 Hz) did not affect food-seeking behaviour (Extended Data Fig. 2g, h).

In contrast to the facilitated food approach, the intake of standard or high-fat food was not changed by gamma-rhythmic LS$_{SST}$–LH opto-stimulation (Fig. 1k, Extended Data Figs 2i, j, 3). Changes to the power of gamma oscillations according to the food approach rate and the latency to enter the food zone during optostimulation were similar between mice with different levels of food intake (see Supplementary Information, Statistical Analysis of Fig. 1f).

Examination of reinforcing properties of the LS$_{SST}$–LH pathway in a real-time place preference model did not reveal a significant preference for the photostimulation-paired chamber (Extended Data Fig. 4a, b). The approach rate to a new or a familiar object did not depend on the power of spontaneous gamma oscillations (Extended Data Fig. 4c, d), and gamma stimulation of the LS$_{SST}$–LH pathway did not facilitate the approach to a novel object (Extended Data Fig. 4e), suggesting a specific involvement of this pathway in food-seeking rather than novelty-processing, which relies on other circuits[24].

To explore the necessity of the LS$_{SST}$–LH pathway for food-seeking behaviour, we optogenetically inhibited the LS$_{SST}$–LH projections during food approach, delivering yellow light (593 nm) on LH projections of LS$_{SST}$ cells (Fig. 1l) expressing the adeno-associated virus AAV- DIO-eNPAC2.0 (see Supplementary Information, Results, Fig. 1m, Extended Data Figs 5, 6a–d), as a mouse moved closer to the food zone, that is, entered the approach zone (Extended Data Fig. 6e). Such behaviour-dependent inhibition of the LS$_{SST}$–LH pathway did not change the running speed (Fig. 1n), but did reduce food-seeking behaviour: a latency to enter the food zone increased (Fig. 1o) whereas the number of entries into the food zone decreased (Fig. 1p).

[1]Behavioural Neurodynamics Group, Leibniz Institute for Molecular Pharmacology (FMP)/ NeuroCure Cluster of Excellence, Berlin, Germany. [2]Department of Bioengineering, Stanford University, Stanford, California 94305, USA. [3]Howard Hughes Medical Institute; Stanford University, Stanford, California 94305, USA. [4]The Francis Crick Institute, Mill Hill Laboratory, London NW7 1AA, UK. [5]Department of Mathematics, Tufts University, Medford, Massachusetts 02155, USA. [6]Department of Psychiatry and Behavioural Sciences, W080 Clark Center, 318 Campus Drive West, Stanford University, Stanford, California 94305, USA.
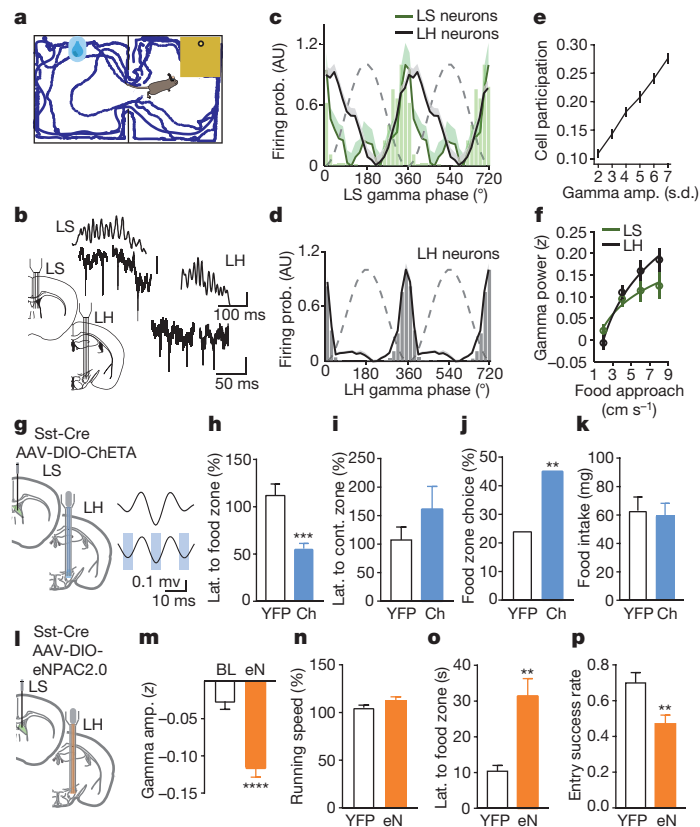*These authors contributed equally to this work.

Figure 1 | Coordinated gamma oscillations in the LS and the LH drive food seeking. a, Recording enclosure. **b**, Signal traces. Scale bar, 0.2 mV. **c**, **d**, The firing probability (scaled from minimum to maximum, arbitrary units, AU) of LS and LH cells during LS gamma oscillations (60–90 Hz) (**c**, LS: $n = 68$ cells, $P < 0.0001$, Rayleigh test; LH cells: $n = 126$, $P < 0.0001$, $n = 5$ mice) and LH gamma oscillations (60–90 Hz) (**d**, $n = 290$ cells, $P < 0.0001$, Rayleigh test; $n = 5$ mice). Histograms denote representative cells. **e**, Participation rate of LS cells during gamma oscillations ($P < 0.00001$, ANOVA). **f**, Gamma power (60–90 Hz) matched the time required to reach the food zone (approach rate LS: $R^2 = 0.95$, LH: $R^2 = 0.99$, logarithmic fits, LS: $n = 13$ mice, $P = 0.000013$; LH: $n = 16$ mice, $P < 0.00001$, ANOVA). **g**, Examples of opto-induced and frequency-matched spontaneous LH gamma, average waveforms. **h–k**, LS$_{SST}$–LH gamma-frequency optostimulation with excitatory opsin ChETA (Ch) reduced latency to enter the food zone (**h**, yellow fluorescent protein

(YFP): $n = 8$ mice, opsin: $n = 10$ mice; $***P = 0.0004$, t-test), but not the control zone (**i**, YFP: $n = 7$ mice, opsin: $n = 8$ mice, $P = 0.3$, t-test), and increased the preference of the food zone over other corners of the enclosure (**j**, YFP: $n = 8$ mice, opsin: $n = 12$ mice, $**P = 0.0047$, binomial test), but did not affect food intake (**k**, YFP: $n = 8$ mice, opsin: $n = 9$ mice, $P = 0.8$, t-test). **l–p**, LS$_{SST}$–LH opto-inhibition with opsin variant eNPAC2.0 (eN) (**l**) decreased gamma amplitude (**m**, baseline (BL) versus inhibition, $n = 33$ recording sessions, 60–90 Hz; $****P < 0.0001$, t-test), did not affect running speed (**n**, YFP: $n = 8$ mice, eN: $n = 8$ mice; $P = 0.11$, t-test), increased the latency to enter the food zone (**o**, YFP: $n = 8$ mice, eN: $n = 8$ mice; $**P = 0.0011$, t-test), and decreased the number of food-zone entries (**p**, YFP: $n = 8$ mice, eN: $n = 8$ mice; $**P = 0.0094$, t-test). Data are mean ± s.e.m. The mouse brain was reproduced with permission from ref. 30.

To investigate the neuronal mechanisms underlying behavioural effects of gamma-rhythmic entrainment of the LH, we analysed the timing of LH neuronal activity during gamma oscillations. Most LH neurons fired preferentially at the trough of the LH gamma oscillation cycle (Fig. 2a, Extended Data Fig. 7a). However, one-quarter of LH cells were inhibited at the trough and fired during the rising phase of the spontaneous gamma oscillation (Fig. 2a, Extended Data Fig. 7a). To study the causal role of the LS gamma input in the oscillatory inhibition of LH cells, we optogenetically stimulated LS–LH projections at gamma frequency while recording LH cells (Fig. 2b, c), and quantified the oscillatory response of each LH cell to the LS–LH stimulation (Fig. 2d–f). LH cells, which rhythmically responded to the LS–LH stimulation, were also more inhibited during troughs of spontaneous gamma oscillations (Fig. 2e, f), that is, at times when LS cells fired the most (Fig. 1c). This suggests that LS inputs inhibit a subset of LH neurons, thus enabling their phase-shifted, temporally separated signalling during gamma oscillations.

We next investigated how the timing of neuronal discharge during gamma oscillations relates to the feeding-related activity of LH cells. The firing of a subset of LH neurons in the free-access feeding model matched the location of the food zone (FZ-match cells), whereas other cells were preferentially active at a distance from the food zone

(FZ-mismatch cells) (Fig. 2g, Extended Data Fig. 7b). FZ-match cells appeared to reduce their firing prominently during the gamma oscillation trough (Fig. 2h), when LH is mostly influenced by the LS inhibition (Fig. 2e, f, h), and fired with an increased probability during the subsequent rising phase of the gamma cycle (Fig. 2h, i). By contrast, FZ-mismatch cells showed high excitability at the gamma trough (Fig. 2i, Extended Data Fig. 7c), characteristic for control of discharge timing by local oscillatory inhibition[13].

To establish further how the LS-driven gamma phase separation affects the activity of LH neurons involved in feeding, we studied gamma oscillatory responses of genetically defined LH cells. Recording of responses of identified Vgat and melanin-concentrating hormone (MCH) LH cells to intracellular injections of gamma oscillatory currents in brain slices (Fig. 2j, Extended Data Fig. 7d–g) revealed a higher magnitude of membrane potential oscillations in Vgat than in MCH cells (Fig. 2j, k). Spike trains of optogenetically tagged presumed LH$_{Vgat}$ cells in behaving mice[25,26] displayed a distinct maximum of rhythmicity at gamma frequencies (Fig. 2l, Extended Data Fig. 7h). Vgat cells are preferentially active either in or outside the food zone[4]—that is, some Vgat cells are FZ-match cells whereas others are FZ-mismatch cells. We therefore analysed the firing of Vgat cells during gamma oscillations in the free-access feeding model. FZ-mismatch Vgat cells fired
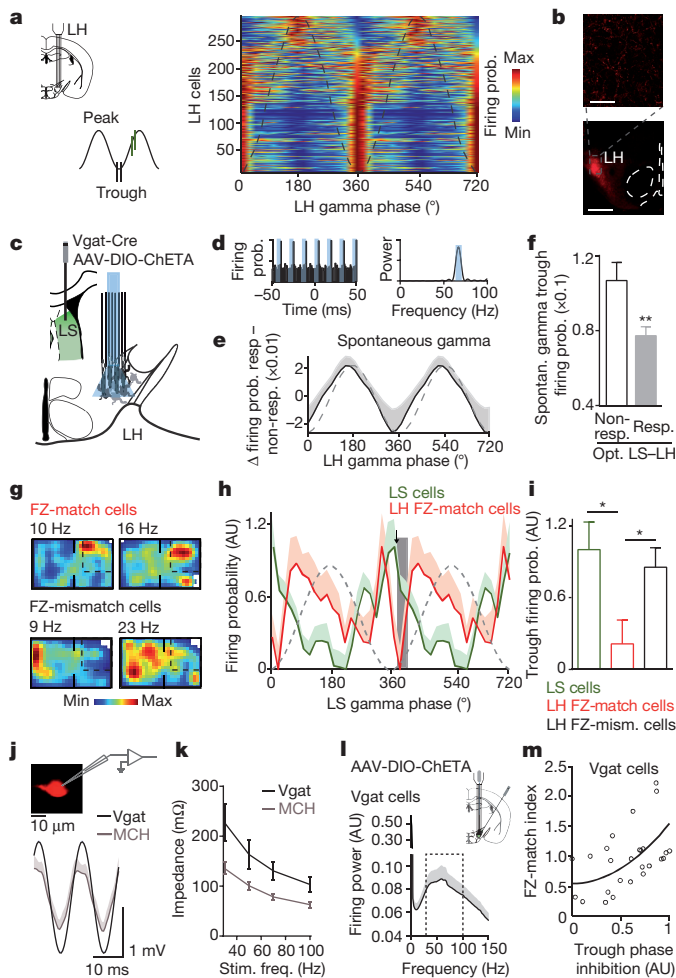
Figure 2 | LS inputs determine separate signalling of feeding-related LH cells during gamma oscillations. a, Firing probability (colour-coded) of LH cells in behaving mice during LH gamma oscillations (60–90 Hz, $n = 290$ cells). **b**, LS_{GABA} fibres in the LH. Scale bars, 50 μm (top) and 500 μm (bottom). **c**, Optostimulation scheme. **d**, Pulse-triggered cross-correlogram and its power spectrum of an LH cell, responsive to LS–LH gamma-rhythmic optostimulation. **e**, Difference in firing probability between responsive and non-responsive cell populations. **f**, Firing during troughs of spontaneous gamma oscillations (responsive: $n = 61$ cells, non-responsive: $n = 15$ cells; **$P = 0.007$, ANOVA). **g**, Example colour-coded maps of firing rate. **h, i**, The firing probability of LH FZ-match cells was reduced at the trough of spontaneous gamma oscillation. Bins marked by the arrow (for LS cells) and the grey shading (for LH cells) were analysed in **i** (30–60 Hz, LS: $n = 69$ cells, LH: $n = 37$ cells; *$P < 0.05$, t-test). **j**, Voltage response of a Vgat and an MCH cell to gamma-frequency (70 Hz) current input. **k**, Subthreshold voltage response of Vgat ($n = 8$) and MCH ($n = 4$) cells to input current (30, 50, 70 and 100 Hz; $P = 0.0018$, ANOVA). **l**, Gamma-rhythmic firing of opto-identified LH_{Vgat} cells ($n = 60$) in behaving mice. **m**, Inhibition during the gamma trough related to FZ-match index of opto-identified LH_{Vgat} cells (30–60 Hz, $n = 26$ cells, Pearson's correlation, $r = 0.49$, $P = 0.012$). Data are mean ± s.e.m. The mouse brain was reproduced with permission from ref. 30.

preferentially during the trough of the gamma oscillation, whereas FZ-match Vgat cells reduced firing during this phase (Fig. 2m). Thus, LS gamma oscillatory input during food seeking enables fine time-scale separation of intrinsically gamma-rhythmic Vgat cells according to their feeding-related activity.

The selective induction of food seeking without changes in food intake by LS–LH gamma-rhythmic stimulation noted above (Fig. 1) contrasts with an increased food intake during somatic optostimulation of LH_{Vgat} cells[4] (Extended Data Fig. 8a–f). To investigate intrahypo-thalamic network responses that underlie differential functions of
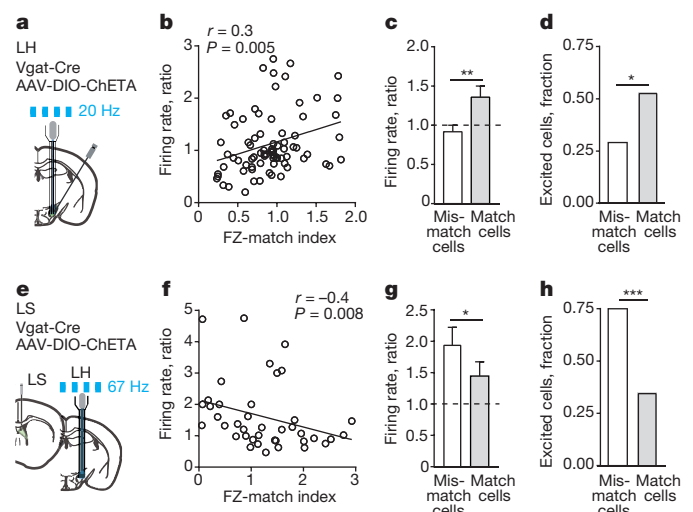

Figure 3 | Intra-LH and LS inhibitory inputs recruit distinct feeding-related LH populations. a, Optostimulation scheme. **b**, Positive correlation of FZ-match index with changes in firing rate during optostimulation of LH_{Vgat} cells ($n = 79$ cells, Spearman correlation, $r = 0.32$, $P = 0.005$). **c**, FZ-match rather than FZ-mismatch cells were activated by optostimulation of LH_{Vgat} cells (mismatch: $n = 31$ cells, match: $n = 15$ cells; **$P = 0.007$, t-test). **d**, Fractions of FZ-mismatch and FZ-match cells excited during optostimulation of LH_{Vgat} cells (*$P = 0.047$, binomial test). **e**, Optostimulation scheme. **f**, Inverse correlation of FZ-match index with changes in firing rate after LS_{Vgat}–LH optostimulation ($n = 41$ cells, Spearman correlation, $r = -0.41$, $P = 0.008$). **g**, FZ-mismatch cells were more strongly activated during LS_{Vgat}–LH optostimulation than were FZ-match cells (mismatch: $n = 12$ cells, match: $n = 20$ cells; *$P = 0.019$, Mann–Whitney test). **h**, Fractions of FZ-mismatch and FZ-match cells excited during LS_{Vgat}–LH optostimulation (***$P = 0.0002$, binomial test). Data are mean ± s.e.m. The mouse brain was reproduced with permission from ref. 30.

LH_{Vgat} cells versus LS–LH projections in feeding behaviour, we studied the effects of these manipulations on the firing of LH neurons. Optostimulation of LH_{Vgat} cells (Fig. 3a, Extended Data Fig. 8g) evoked a prominent increase in the firing of FZ-match but not FZ-mismatch neurons (Fig. 3b–d, Supplementary Information, Statistical Analysis). By contrast, gamma-frequency optogenetic stimulation of LS–LH projections (Fig. 3e, Extended Data Fig. 8h) increased the firing of FZ-mismatch rather than FZ-match neurons (Fig. 3f–h). Thus, separate activation of these two populations during gamma oscillations (Fig. 2) is associated with an increased firing rate of FZ-mismatch cells and leads to food seeking, whereas the activation of FZ-match cells facilitates food intake.

Next, we investigated the circuitry upstream from LS providing top-down forebrain signalling to the LH. A biophysical network model demonstrated that the LS displayed a prominent gamma rhythm that was further stabilized by external gamma input (see Supplementary Results and Extended Data Fig. 9a–d). Since the LS receives inputs from the medial prefrontal cortex (mPFC) and the hippocampus[23], both of which exhibit gamma oscillations, we studied the coordination of gamma oscillations in the LS with each of these regions using double- and triple-site recordings (Fig. 4a, Extended Data Fig. 9e). While LS and hippocampus are coordinated in the theta band (5–10 Hz)[22], they were weakly coherent at gamma frequencies (Fig. 4b, Extended Data Fig. 9f–h). Conversely, we found co-occurrence of intermittent gamma LFP epochs in the LS and mPFC (Fig. 4a) and increased gamma-band coherence of a local LS activity parameter, current flow density, with LFP in the mPFC (Fig. 4b, Extended Data Fig. 9f–h).

In contrast to a well-established innervation of the LS by the hippocampus[8], little is known about inputs from the mPFC. CLARITY[27], an intact brain analysis, revealed prominent fibres of CaMKIIa-expressing mPFC neurons in the LS (Fig. 4c, d). Posterior to the LS
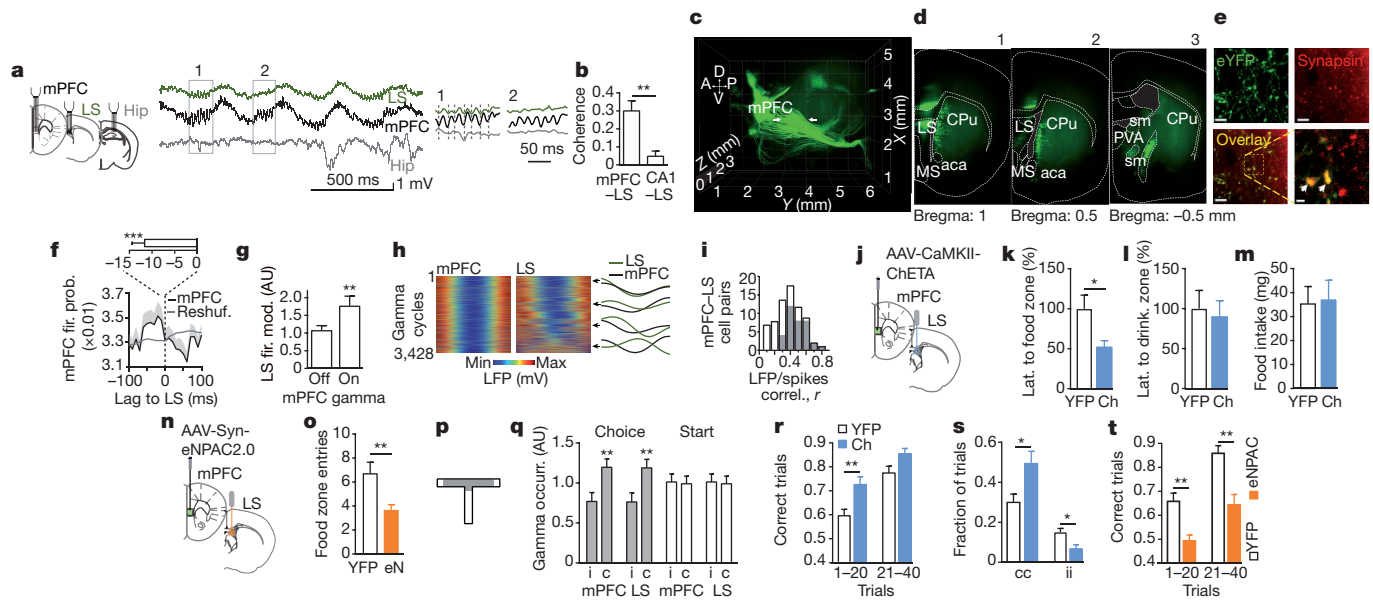
Figure 4 | Gamma-rhythmic mPFC–LS signalling improves performance in a food-rewarded learning task. a, Triple-site LFP recording. **b**, Interregional gamma-band coherence (30–90 Hz, mPFC–LS: $n = 8$ mice, CA1–LS: $n = 6$ mice; **$P = 0.0027$, Mann–Whitney test). **c**, Example 3D CLARITY image (1 out of 6 mice), showing enhanced YFP (eYFP)-expressing mPFC neuron projections. Arrows denote LS. A, anterior; D, dorsal; P, posterior; V, ventral. **d**, mPFC projections in the LS (1, 2). aca, anterior part of anterior commissure; CPu, caudate putamen; MS, medial septum; sm, stria medullaris. **e**, Representative images (1 out of 3 mice) of eYFP-expressing mPFC fibres in the LS, counterstained with anti-synapsin antibody. Scale bars, 5 μm, 1 μm (inset). **f**, Cross-correlation of neuronal discharge in the mPFC and LS; reference are LS spikes during gamma oscillation (156 cell pairs). Bar chart (top) denotes average lag of mPFC cell firing probability peaks (***$P < 0.0001$, t-test). **g**, Local gamma modulation of LS cells during mPFC gamma oscillations ('on'), compared with 'off' episodes (normalized circular resultant vector (r) length: **$P = 0.0069$, t-test). **h**, mPFC gamma oscillation cycles and corresponding excerpts of LS gamma LFP; amplitude is colour-coded. Example cycles are shown on the right. **i**, Distribution of correlation coefficients between LS and mPFC spike lags versus gamma LFP phase lags (grey bars denote cells with correlations $P < 0.05$, 35 out of 71 cell pairs). **j–m**, Gamma-rhythmic mPFC–LS optostimulation with ChETA or

ChR2 (Ch) (**j**) reduced latency to enter the food zone (**k**, YFP: $n = 8$ mice, opsin: $n = 7$ mice; *$P = 0.03$, t-test) but not the drinking zone (**l**, YFP: $n = 8$ mice, opsin: $n = 7$ mice; $P = 0.7$, t-test), and did not affect food intake (**m**, YFP: $n = 7$ mice, opsin: $n = 7$ mice; $P = 0.9$, t-test). **n**, **o**, Inhibition of the mPFC–LS pathway with eNPAC2.0 (**n**) reduced the number of entries into the food zone (**o**, YFP: $n = 8$ mice, opsin: $n = 6$ mice; **$P = 0.008$, Mann–Whitney test). **p**, T-maze scheme. **q**, The occurrence of spontaneous mPFC and LS gamma (60–90 Hz) episodes in the choice segment of the T-maze ($n = 4$ mice; mPFC: **$P = 0.002$, LS: **$P = 0.002$, ANOVA), and the start arm of the T-maze ($n = 4$ mice; $P = 0.97$, ANOVA). c, correct trials, i, incorrect trials. **r**, **s**, mPFC–LS gamma optostimulation with ChETA or ChR2 increased the number of correct choices in the T-maze (**r**, trials 1–20: YFP: $n = 7$ mice, opsin: $n = 9$ mice; **$P = 0.0096$, t-test; trials 21–40: YFP: $n = 6$ mice, opsin: $n = 5$ mice; $P = 0.074$, t-test), increased the repeated correct trials (**s**, cc, YFP: $n = 7$ mice, opsin: $n = 9$ mice; *$P = 0.026$, t-test) and decreased the repeated incorrect trials (**s**, ii, YFP: $n = 7$ mice, opsin: $n = 9$ mice; *$P = 0.014$, t-test). **t**, mPFC–LS inhibition with eNPAC2.0 decreased the number of correct choices in the T-maze (trials 1–20: YFP: $n = 7$, opsin: $n = 7$; **$P = 0.0016$; trials 21–40: YFP: $n = 7$, opsin: $n = 6$; **$P = 0.0018$, t-test). Data are mean ± s.e.m. The mouse brain was reproduced with permission from ref. 30.

no fibres of passage were present, indicating that mPFC projections terminate in the LS (Fig. 4c, d, Extended Data Fig. 9i, Supplementary Video 1). We further confirmed termination of mPFC fibres in the LS using the synaptic markers synapsin (Fig. 4e, Extended Data Fig. 9j) and synaptophysin (Extended Data Fig. 9k).

Coordination of gamma oscillations between the mPFC and the LS was accompanied by the interregional coordination of neuronal activity. The firing of LS cells during gamma oscillations was preceded by an increased discharge of mPFC neurons by approximately 11 ms (Fig. 4f). A population of mPFC cells rhythmically changed firing probability according to the phase of the LS oscillation, and preceded the maximal discharge of the LS population by around 90° (Extended Data Fig. 10a). The firing of LS neurons was better entrained by local gamma oscillations in the presence of gamma oscillations in the mPFC (Fig. 4g). The precision of co-firing between LS and mPFC predicted phase lags between concurrent LFP gamma cycles in these regions: a better correspondence of the LFP oscillation phases was associated with a more precise coordination of discharge phases in half of the mPFC–LS cell pairs (Fig. 4h, i and Supplementary Information, Statistical Analysis).

To address the function of mPFC–LS gamma-rhythmic signalling in food-seeking behaviour, we targeted excitatory opsins (ChR2 or ChETA) to CaMKIIa-expressing cells in the mPFC, and stimulated their projections in the LS at gamma frequency (Fig. 4j, Extended

Data Fig. 10b, c) in the free-feeding model. The stimulation facilitated food approach, shortening latency to reach the food zone (Fig. 4k) but not the drinking zone (Fig. 4l) or a control zone (Extended Data Fig. 10d), without concomitant changes in running speed (Extended Data Fig. 10e) or food intake (Fig. 4m). In accordance, inhibition of the mPFC–LS pathway (Fig. 4n) during the food approach decreased the number of entries in the food zone (Fig. 4o). To study the role of gamma signalling in the mPFC–LS pathway in a cognitive, food-reinforced task, we used an mPFC-dependent[28] and LH-dependent[29] delayed nonmatching-to-place (T-maze) task (Fig. 4p). Recordings from the mPFC and LS as the mice performed the task revealed that correct choices were associated with an increased count of fast (60–90 Hz) and slow (30–60 Hz) gamma oscillation episodes in the mPFC and LS during the choice phase of the task and subsequent food approach, but not in the start arm of the T-maze (Fig. 4q, Extended Data Fig. 10f). During optogenetic stimulation of mPFC–LS projections at gamma frequency, the number of correct trials increased in opsin-expressing mice compared to control mice (Fig. 4r). Stimulation also improved temporal stability of performance, increasing the fraction of repeated correct trials while decreasing the fraction of repeated incorrect trials (Fig. 4s). Gamma-rhythmic mPFC–LS optostimulation in water-restricted mice using water as a reward also increased the number of correct trials (Extended Data Fig. 10g) and a fraction of the repeated

correct trials (Extended Data Fig. 10h). Theta-frequency stimulation of mPFC–LS projections did not affect performance in the T-maze task (Extended Data Fig. 10i, j). Optogenetic inhibition of the mPFC–LS pathway led to a decreased number of correct trials in eNPAC2.0-expressing mice compared to control mice (Fig. 4t). This suggests that gamma signalling within the mPFC–LS pathway regulates food-seeking behaviour and contributes to successful performance in a goal-directed cognitive task.

Our study identifies a top-down pathway from the mPFC via the LS to the LH, which uses gamma oscillations to regulate food seeking. Our results indicate that signalling by LH cells with distinct feeding-related activity is temporally separated and amplified by gamma-rhythmic inhibition from the LS, the temporal precision of which is coordinated with gamma oscillations in mPFC. Regulation of motivated behaviour by this circuit makes it a promising target for innovative therapies.

1. Saper, C. B., Chou, T. C. & Elmquist, J. K. The need to feed: homeostatic and hedonic control of eating. *Neuron* **36**, 199–211 (2002).
2. Waterson, M. J. & Horvath, T. L. Neuronal regulation of energy homeostasis: beyond the hypothalamus and feeding. *Cell Metab.* **22**, 962–970 (2015).
3. Steculorum, S. M. *et al.* Hypothalamic UDP increases in obesity and promotes feeding via P2Y6-dependent activation of AgRP neurons. *Cell* **162**, 1404–1417 (2015).
4. Jennings, J. H. *et al.* Visualizing hypothalamic network dynamics for appetitive and consummatory behaviors. *Cell* **160**, 516–527 (2015).
5. Rolls, E. T., Burton, M. J. & Mora, F. Hypothalamic neuronal responses associated with the sight of food. *Brain Res.* **111**, 53–66 (1976).
6. Chen, Y., Lin, Y. C., Kuo, T. W. & Knight, Z. A. Sensory detection of food rapidly modulates arcuate feeding circuits. *Cell* **160**, 829–841 (2015).
7. Mileykovskiy, B. Y., Kiyashchenko, L. I. & Siegel, J. M. Behavioral correlates of activity in identified hypocretin/orexin neurons. *Neuron* **46**, 787–798 (2005).
8. Risold, P. Y. & Swanson, L. W. Structural evidence for functional domains in the rat hippocampus. *Science* **272**, 1484–1486 (1996).
9. Tse, D. *et al.* Schema-dependent gene activation and memory encoding in neocortex. *Science* **333**, 891–895 (2011).
10. Euston, D. R., Gruber, A. J. & McNaughton, B. L. The role of medial prefrontal cortex in memory and decision making. *Neuron* **76**, 1057–1070 (2012).
11. Gray, C. M. & Singer, W. Stimulus-specific neuronal oscillations in orientation columns of cat visual cortex. *Proc. Natl Acad. Sci. USA* **86**, 1698–1702 (1989).
12. Salinas, E. & Sejnowski, T. J. Correlated neuronal activity and the flow of neural information. *Nat. Rev. Neurosci.* **2**, 539–550 (2001).
13. Csicsvari, J., Jamieson, B., Wise, K. D. & Buzsáki, G. Mechanisms of gamma oscillations in the hippocampus of the behaving rat. *Neuron* **37**, 311–322 (2003).
14. Fries, P. Rhythms for cognition: communication through coherence. *Neuron* **88**, 220–235 (2015).
15. Colgin, L. L. *et al.* Frequency of gamma oscillations routes flow of information in the hippocampus. *Nature* **462**, 353–357 (2009).
16. Yamamoto, J., Suh, J., Takeuchi, D. & Tonegawa, S. Successful execution of working memory linked to synchronized high-frequency gamma oscillations. *Cell* **157**, 845–857 (2014).
17. Igarashi, K. M., Lu, L., Colgin, L. L., Moser, M. B. & Moser, E. I. Coordination of entorhinal-hippocampal ensemble activity during associative learning. *Nature* **510**, 143–147 (2014).
18. Kim, H., Ährlund-Richter, S., Wang, X., Deisseroth, K. & Carlén, M. Prefrontal parvalbumin neurons in control of attention. *Cell* **164**, 208–218 (2016).
19. Cho, K. K. *et al.* Gamma rhythms link prefrontal interneuron dysfunction with cognitive inflexibility in *Dlx5/6*$^{+/-}$ mice. *Neuron* **85**, 1332–1343 (2015).
20. Cardin, J. A. *et al.* Driving fast-spiking cells induces gamma rhythm and controls sensory responses. *Nature* **459**, 663–667 (2009).
21. Sartor, G. C. & Aston-Jones, G. S. A septal-hypothalamic pathway drives orexin neurons, which is necessary for conditioned cocaine preference. *J. Neurosci.* **32**, 4623–4631 (2012).
22. Bender, F. *et al.* Theta oscillations regulate the speed of locomotion via a hippocampus to lateral septum pathway. *Nat. Commun.* **6**, 8521 (2015).
23. Sheehan, T. P., Chambers, R. A. & Russell, D. S. Regulation of affect by the lateral septum: implications for neuropsychiatry. *Brain Res. Brain Res. Rev.* **46**, 71–117 (2004).
24. Takeuchi, T. *et al.* Locus coeruleus and dopaminergic consolidation of everyday memory. *Nature* **537**, 357–362 (2016).
25. Nieh, E. H. *et al.* Decoding neural circuits that control compulsive sucrose seeking. *Cell* **160**, 528–541 (2015).
26. Herrera, C. G. *et al.* Hypothalamic feedforward inhibition of thalamocortical network controls arousal and consciousness. *Nat. Neurosci.* **19**, 290–298 (2016).
27. Ye, L. *et al.* Wiring and molecular features of prefrontal ensembles representing distinct experiences. *Cell* **165**, 1776–1788 (2016).
28. Spellman, T. *et al.* Hippocampal-prefrontal input supports spatial encoding in working memory. *Nature* **522**, 309–314 (2015).
29. Mendelson, J. & Chorover, S. L. Lateral hypothalamic stimulation in satiated rats: T-maze learning for food. *Science* **149**, 559–561 (1965).
30. Paxinos, G. & Franklin, K. B. J. *The Mouse Brain in Stereotaxic Coordinates* (Elsevier Academic Press, 2001).

Author Contributions M.C.-C., F.B., S.V., Y.H., N.D., F.R., E.V., A.P. and T.K. performed electrophysiological and optogenetic experiments *in vivo*; M.G., A.P., M.C.-C. and T.K. performed analysis of *in vivo* data, L.Y. performed CLARITY experiments; C.K. performed electrophysiological recordings in brain slices; C.B. designed and performed computational modelling; S.Y.L. performed electrophysiological recordings in brain cultures, C.R. designed and made an opsin construct; D.B. designed and supervised experiments in brain slices; K.D. designed and supervised CLARITY experiments and the development of optogenetic tools; A.P. and T.K. originated and designed the project and supervised *in vivo* part; and A.P and T.K. wrote the manuscript with the input from all co-authors.

Author Information Reprints and permissions information is available at www.nature.com/reprints. The authors declare no competing financial interests. Readers are welcome to comment on the online version of the paper. Correspondence and requests for materials should be addressed to A.P. (ponomarenko@fmp-berlin.de) or T.K. (korotkova@fmp-berlin.de).

METHODS

Experimental subjects. Vgat-ires-Cre[31], Sst-Cre[32] and PV-Cre[33] knock-in mice (The Jackson Laboratory, Bar Harbour) and C57BL/6 male mice, 10–25 weeks old, were used. Mice were housed under standard conditions in the animal facility and kept on a 12 h light/dark cycle. All procedures were performed in accordance with national and international guidelines, and were approved by the local health authority (Landesamt für Gesundheit und Soziales, Berlin) and the Stanford University Institutional Animal Care and Use Committee.

Virus injections. Injections were performed as described previously[22,34]. Mice were anaesthetized with isoflurane and placed in a stereotaxic head frame (David Kopf Instruments). A 34-gauge bevelled metal needle connected via a tube with a microsyringe pump (PHD Ultra, Harvard Apparatus) was used to infuse viruses at a rate of 100 nl min^{-1}. After infusion, the needle was kept at the injection site for 10 min and then slowly withdrawn before the incision was sutured. Optogenetic constructs from K. Deisseroth, purchased from Penn Vector Core, UNC Gene Therapy Center Vector Core, or provided by K. Deisseroth, were used. For manipulations of the LS–LH pathway, Vgat-Cre mice were injected bilaterally in the LS (right: anterior-posterior (AP) 0.74, lateral (L) 0.38, ventral (V) 3.3; 3.1 mm; left: AP 0.62, L 0.33, V 3.45; 3.0 mm) with 0.3 μl per injection site of AAV2/5-Ef1a-DIO-ChETA(E123T/H13R)-eYFP-WPRE-hGH (Penn Vector Core, titre 1.75×10^{12} viral genomes (vg) per ml). Sst-Cre mice were injected bilaterally in the LS (right: AP 0.38, L 0.4, DV 3.0, 2.7 mm; left: AP 0.26, L 0.4, V 3.0, 2.5 mm) with 0.125–0.25 μl per injection site of AAV2/5-Ef1a-DIO-ChETA(E123T/H13R)-eYFP-WPRE-hGH, titre 1.75×10^{12} vg ml^{-1} (Penn Vector Core) or 0.2 μl per injection site of AAVdj-nEF-DIO-NpHR-TS-p2A-hChR2(H134R)-eYFP (eNPAC2.0, titre 6.1×10^{12} vg ml^{-1}) or 0.125–0.2 μl per injection site of AAV2-EF1a-DIO-eYFP-WPRE-hGH (Penn Vector Core, titre 2×10^{12} vg ml^{-1}). For manipulation of LH$_{Vgat}$ cells, Vgat-Cre mice were injected bilaterally in the LH (AP −1.5, L ±1, V 5.4 mm) with 0.3 μl per injection site of AAV2/5-Ef1a-DIO-ChETA(E123T/H13R)-eYFP-WPRE-hGH (Penn Vector Core) or 0.3 μl per injection site of AAVdj-nEF-DIO-NpHR-TS-p2A-hChR2(H134R)-eYFP (eNPAC2.0, titre 6.1×10^{12} vg ml^{-1}) or 0.3 μl per injection site of AAV2-EF1a-DIO-eYFP-WPRE-hGH (Penn Vector Core, titre 2×10^{12} vg ml^{-1}). For manipulations of the mPFC–LH pathway, mice were bilaterally injected in the mPFC (AP 1.70, L ±0.35, V 2.85 mm) with 0.25–0.5 μl per injection site of AAV2-CaMKIIa-hChR2(H134R)-eYFP (Penn Vector Core, titre 2.55×10^{12} vg ml^{-1}) or 0.25–0.5 μl per injection site of AAV5-CaMKIIa-ChETA(E123T/H134R)-eYFP-WPRE-hGH (Penn Vector Core, titre 1.26×10^{13} vg ml^{-1}), or 0.25–0.5 μl per injection site of (AAVdj-hSyn-NpHR-TS-p2A-hChR2(H134R)-eYFP (eNPAC2.0, titre 2.9×10^{13} vg ml^{-1}) or 0.5 μl per injection site of AAV2-CaMKIIa-eYFP (University of North Carolina Vector Core, titre 5×10^{12} vg ml^{-1}). For CLARITY experiments, mice were injected in the mPFC (AP 2.0, L 0.3, V 2.6 mm) with 1 μl AAV8-CaMKIIa-eYFP-NRN. For synaptophysin imaging, 1 μl AAV8-CaMKIIa-synaptophysin-mCherry (7×10^{13}), was injected in the mPFC (AP 2.0, L 0.3, V 2.6 mm).

Implantations of optic fibres and electrodes. Optic fibre implants were fabricated from 100 μm diameter fibre (0.22 numerical aperture (NA), Thorlabs) and zirconia ferrules (Precision Fibre Products). For optogenetic manipulations of mPFC–LS pathway, mice were implanted with optic fibre implants on top of the LS (right, AP 0.1, L 0.25, V 2.25 mm, left, AP 0.5, L 0.3, V 2.7 mm). For optogenetic manipulations in the LH, optical fibres were bilaterally (for LS–LH and LH stimulation or inhibition) or unilaterally (LH stimulation combined with the LH silicon probe recordings) implanted above the LH (AP −1.6, L 1, V 4.8 mm). Arrays of single tungsten wires (40 μm, California Fine Wire Company), stationary implanted linear silicon probes (CM32, NeuroNexus Technologies), or movable probes (B32 or B64, NeuroNexus Technologies) mounted on a microdrive[35] were implanted as described previously[22,26]. The following coordinates were used for electrode implantations in the LS: AP 0–0.5, L 0.2–0.45, V 2.3–3.4 mm (B32 probes, B64 probes (mPFC–LS co-implantations), CM32, wire arrays); LH: AP −1.6, L 1, V 4.7 mm (B32 probes, B64 probe, wire arrays); mPFC: AP 1.4–1.9, L 0.3, V 3.0 mm (B64 probes (mPFC–LS co-implantations), wire arrays); dorsal hip: AP −2.1, L 1.6, V 1.5 mm (wire arrays), ventral hip: AP −3.16, L 2.5–3.5, V 4.0 mm (wire arrays). Reference and ground electrodes were miniature stainless-steel screws in the skull above the cerebellum. The implants were secured on the skull with dental acrylic.

Data acquisition. Electrodes were connected to operational amplifiers (HS-8, Neuralynx, or Noted BT) to eliminate cable movement artefacts. Electrophysiological signals were differentially amplified, band-pass filtered (1 Hz–10 kHz, Digital Lynx, Neuralynx) and acquired continuously at 32 kHz. A light-emitting diode was attached to the headset to track the mouse's position (at 25 Hz). Timestamps of laser pulses were recorded together with electrophysiological signals.

Optogenetic stimulation. A 3-m-long fibreoptic patch cord with protective tubing (Thorlabs) was connected to a chronically implanted optical fibre with a zirconia sleeve (Precision Fibre Products), which allowed the mice to explore an enclosure freely or perform a behavioural task during optogenetic manipulations. Subjects were randomly assigned to the experimental conditions. For optogenetic stimulation, the patch cord was connected to a 473-nm diode-pumped solid-state laser (R471005FX, Laserglow Technologies) with an FC/PC adaptor. The laser output was controlled using a stimulus generator and MC_Stimulus software (Multichannel Systems). Optogenetic stimulation of LS–LH and mPFC–LS projections consisted of 5 ms blue (473 nm) light pulses, at 66.7 Hz or a control, non-gamma (theta) intensity-matched stimulation (167 Hz bursts of 4 ms pulses repeated at 9 Hz) with the light power output (during light-on parts of illumination cycles) of 10–25 mW from the tip of the patch cord measured with a power meter (PM100D, Thorlabs). Optogenetic stimulation of LH somata consisted of 5 ms blue (473 nm) light pulses, at 20 Hz, with light power output (during light-on parts of illumination cycles) of 10–25 mW from the tip of the patch cord. For bilateral optogenetic inhibition, optic fibre implants were connected via patch cords to a 593-nm diode-pumped solid-state laser (R591005FX, Laserglow Technologies) using a multimode fibre optic coupler (FCMM50-50A-FC, Thorlabs), continuous yellow light, approximately 20 mW from the tip of each patch cord. Duration of light delivery is described below for each type of behavioural experiment. For control experiments, mice expressing YFP in the same brain regions (mPFC or LS) were used, and optostimulation was performed as described above. For within-animal comparisons in sessions in which food intake was measured during LH$_{Vgat}$ stimulation (Extended Data Figs 2i, 8c, d, f), optic patch cords were connected to dummy ferrules, attached to the headset, and light of the same wavelength and power as during opsin-activating stimulation was delivered.

Behavioural assays. *Free-access feeding model.* This was performed in a chamber similar to that described previously[36] (Fig. 1a). Mice freely explored a custom two-chamber (30 × 50 × 20 cm) enclosure, which contained food and water in designated areas (each area 10 × 10 cm; see Fig. 1a). Food (Dustless Precision Pellets, 20 mg, Rodent Purified Diet, Bio Serv) was provided either in a food cup or in a pellet feeder (Coulbourn Instruments Pellet Feeder H14-23M; sampling rate 10 Hz, one nose poke led to the delivery of one food pellet). Before experiments, mice received these pellets in the homecage for at least 2 days, and were habituated to the behavioural setup for at least 3 days. Coordinates of 10 × 10 cm food, drinking, non-food corner zones and a control zone located in the non-food compartment were defined. Times of entering and leaving each zone were extracted from the mouse's position-tracking data. An approach rate was defined as the distance between a position of the mouse and the centre of the food zone, the drinking zone or the control zone, divided by the time it took to enter a respective zone. For each experiment, a corner zone, one of which was a food zone, visited first after the onset of stimulation was detected. Latency to enter each zone was defined as the time between the beginning of optogenetic stimulation and the first entry of the mouse into a zone, with the mouse staying in the zone for at least 1 s. To account for differences in distances to a zone after the stimulation onset, in each experiment we have normalized the latency after stimulation onset to the average latency of entering the same zone from the same distance during the baseline. Duration of experimental sessions and optogenetic manipulations are described below.

Optogenetic activation of LS$_{SST}$–LH projections. Mice explored the enclosure for 30 min: 10 min before stimulation, 10 min during optogenetic stimulation, 10 min after stimulation. Blue light (473 nm) was bilaterally delivered over LS–LH projections, in 5 ms pulses at 66.7 Hz or using a control, non-gamma (theta) intensity-matched stimulation (167 Hz bursts of 4 ms pulses repeated at 9 Hz), with light power output of 10–25 mW. For brief gamma stimulation, 5 ms pulses at 66.7 Hz were delivered for 30 s, followed by a break of 2 min, during a 10 min period.

Optogenetic inhibition of LS$_{SST}$–LH projections during food approach. Mice explored the enclosure for 30 min. Each time the mouse crossed the border of a food-approach area (20 × 20 cm, marked as an orange dotted line on Extended Data Fig. 6e), continuous yellow (593 nm) light was bilaterally delivered over LS–LH projections. Light delivery stopped each time a mouse left the approach zone.

Optogenetic activation of LS$_{SST}$–LH projections during free-access to high-fat food. Mice explored the enclosure for 20 min. Blue light (473 nm) was bilaterally delivered over LS–LH projections, in 5 ms pulses at 66.7 Hz, with light power output of 10–25 mW. High-fat food pellets (Testdiet, 60% energy from fat) were weighted before and after the experiment, to calculate the amount of food (>5 mg) consumed per session.

Optogenetic stimulation of LH$_{Vgat}$ cells. Mice explored the enclosure for 30 or 60 min: 10 or 20 min before stimulation, 10 or 20 min during optogenetic or control light stimulation, 10 or 20 min after stimulation, Dustless precision pellets (BioServ) were counted to measure the amount of food (>1 pellet) consumed per session. Blue light (473 nm) was delivered bilaterally, in 5 ms pulses at 20 Hz.

Optogenetic inhibition of LH$_{Vgat}$ cells in food-deprived mice. Mice received approximately 2.5–3.0 g of standard chow daily; the mouse weight was controlled and weight loss did not exceed 10%. Dustless precision pellets (BioServ) were counted to measure the amount of food consumed by hungry mice (>3 pellets in baseline)

per session. The experiments consisted of four epochs: 10 min light-on (optogenetic or control stimulation), 10 min light-off, 10 min light-on, and 10 min light-off.

Novel object task. This was performed in a custom two-chamber enclosure similar to the one used for the free-feeding model ($30 \times 50 \times 20$ cm). One of the chambers contained a familiar object, whereas the other contained a new object. Before experiments, mice were habituated to the enclosure containing two objects, then for each experimental session one of the objects (new object) was replaced, whereas the object in the other chamber (familiar object) remained the same. Optogenetic stimulation started as the mouse was put in the enclosure. Mice freely explored the enclosure maximally for 2 min, otherwise a session was finished once the mouse visited both objects. Blue light (473 nm) was bilaterally delivered over LS–LH projections, in 5 ms pulses at 66.7 Hz, with light power output of 10–25 mW.

T-maze. Spatial non-matching to place testing on the T-maze was performed as described elsewhere[37]. The T-maze (start arm: $46 \times 11 \times 10$ cm, choice arm: $80 \times 11 \times 10$ cm; see Fig. 4p) was made of pieces of wood painted dark-grey. For spatial non-matching to place testing, each trial consisted of a sample run and a choice run. During the sample run, mice could run only to one arm (left or right, according to a pseudorandom sequence with equal numbers of left and right turns per session) because another arm was blocked by a wooden block. A reward (0.1 ml condensed milk or a 20 mg food pellet) was available in the food well at the end of the arm. After the sample run, mice stayed in another, familiar, enclosure for 10–15 s. The block was then removed, and mice were placed at the end of the start arm to perform the test run. Mice were rewarded for choosing the previously unvisited arm (that is, for alternating). For this test and all subsequent experiments, entry into an arm was defined as when a mouse had placed all four paws into the arm. Mice ran one trial at a time with inter-trial intervals of 3–5 min. Each mouse conducted 20–40 trials in total (10 trials per day). For a subset of experiments, mice were water-restricted and water was used as a reward instead of food. A number of slow (30–60 Hz) or fast (60–90 Hz) gamma-oscillation episodes (detected as described below) in the start or choice arm was normalized by dividing by the mean number of gamma events in each arm during the whole experiment.

Optogenetic activation or inhibition of mPFC–LS projections in the T-maze. Optogenetic stimulation started as the mouse was put at the end of the start arm, and finished when the mouse reached the reward. Blue light was delivered on mPFC–LS projections in 5-ms pulses at 66.7 Hz, or in a non-gamma (theta) intensity-matched stimulation protocol, described above for free-feeding model. For inhibition, yellow light was delivered onto mPFC–LS projections continuously during the run.

Analysis of *in vivo* electrophysiological data. LFP was obtained by down-sampling of the wide-band signal to 1,250 Hz using Neurophysiological Data Manager[38] (http://neurosuite.sourceforge.net/). Gamma oscillations were detected at 30–60 Hz, 60–90 Hz and, for the analysis shown in Extended Data Fig. 1i, 90–120 Hz, bandpass filtered, rectified and smoothed with a 15-ms window LFP signals. Events with amplitudes exceeding 2 s.d. above mean for at least 25 ms were detected[13]. The beginning and the end of oscillatory epochs were marked at points at which the amplitude fell below 1 s.d.

Power spectral density and coherence were computed using the multitaper method (NW = 3). For the analysis of association between gamma power and approach rate, the cumulative power in the 30–60 and 60–90 Hz bands as well as the approach rate (see 'Behavioural assays') was computed, and for each 1-s recording epoch, gamma power was z-transformed. Values within 10 s before entry in the food or drinking zones were statistically evaluated.

Current source density (CSD) maps (versus time and depth) were computed as previously described[37,39]. LFP depth profiles, recorded using CM32 probes with the spatial sampling of 100 μm, were averaged using peak gamma oscillations detected in an LS channel as triggers. The second spatial derivative of the obtained voltage traces, that is, CSD, indicates locations of current sinks and sources in the extracellular space[40]. For the analysis of mPFC–LS and hippocampus–LS coherence, normalized current flow density in the LS was computed by subtraction of gamma-band filtered LFP signals, recorded by a pair of wire electrodes in the LS against a common screw-reference above cerebellum[40,41].

Action potentials were detected in a high-pass filtered signal using NDManager[16] (http://neurosuite.sourceforge.net/). Spike waveforms were extracted and represented by the first three principle components and by amplitudes of action potentials. Spike sorting was performed automatically using KlustaKwik[42] (http://klusta-team.github.io/klustakwik/) followed by manual clusters adjustment using Klusters[38]. Isolation distance[42] was computed for sorted units (LH: 101.5 ± 8.0, LS: 66.3 ± 4.6, mPFC: 56.3 ± 3.6).

Phase of gamma oscillations was computed for signal epochs within detected gamma episodes as described elsewhere[37,43]. In brief, 0° and 360° were assigned to troughs of each gamma cycle and 180° to a cycle peak, phases for each data sample between these points were computed using linear interpolation[13,37]. Subsequently, gamma phases were obtained for data samples when action potentials were emitted,

for each recorded neuron, and firing phase histograms were computed. A possible asymmetry of oscillation cycles leads to a different number of phase samples composing ascending and descending parts of the cycle and can bias firing phase histograms[39]. To prevent this, we tested uniformity of grand gamma phase distributions for each recording using the Rayleigh test and, if significantly non-uniform, computed a deviation of a grand phase histogram from uniformity, via division by the average across all bins. In such recordings, firing histograms were normalized by the corrected grand phase histogram[37,44,45]. Each firing phase histogram was normalized by its total number of spikes. Circular uniformity, mean phase and the resultant vector length were estimated for each histogram. Before averaging, individual histograms were convolved with the Gaussian kernel[46] of size 0.65 s.d.

Putative LH_{Vgat} neurons were optogenetically identified based on rapid (<10 ms lags in laser pulse onset-triggered cross-correlations, computed with 1-ms bins) increase of firing after onset of laser pulses. Reliability of light-induced responses was estimated as a probability of the maximal light-induced spike count in a Poisson distribution computed for cross-correlogram (CCG) delays in the pre-pulse baseline[26,47].

To estimate gamma-rhythmic responses of LH cells to LS–LH stimulation, a cross-correlation (CCG) with the times of LS–LH light stimulation was computed for each cell. To avoid spurious CCG peaks at the stimulation frequency, every second time stamp of light was used as a trigger. A reshuffled CCG was computed using light times shifted to a baseline, light-off, recording epoch. A power spectrum of the response of a cell was then obtained by subtracting the power spectrum of the reshuffled CCG from the power spectrum of the stimulation CCG.

Firing of LH neurons in the free-access feeding model was evaluated as described elsewhere for quantification of positional firing[37,48]. Firing maps were computed by dividing the number of spikes in a given spatial pixel (2×2 cm) by the time spent in this pixel. Periods of immobility (speed <3 cm s^{-1}) were excluded from the analysis. Peak firing rate was defined as the maximum firing rate over all pixels in the environment. For calculation of food-zone preference (FZ-match index), the average firing rate of a cell in the food zone was divided by the average firing rate in a control zone of the same size (10×10 cm), located in the non-food compartment of the enclosure. For the analysis of firing during gamma oscillations, cells were split in 'FZ-match' or 'FZ-mismatch' groups based on an FZ-match index higher or lower than 1, respectively.

For identification of LH cells, excited in response to LH_{Vgat} or LS_{Vgat}–LH optogenetic stimulation, the number of spikes (x) was computed for each 100-ms bin during the baseline (10 min) and within 3 s after stimulation onset. A distribution derived from the baseline was fitted to a Poisson distribution, and rate parameter λ was estimated. A bin with maximal count of spikes during stimulation was assigned to observed value x_{st}. P value was defined as $P(x \geq x_{st})$, in which x follows Pois(λ). The firing rate ratio (R) between 3 s baseline and stimulation epochs was computed for each stimulation epoch and then averaged across stimulation epochs. A cell was classified as excited if $P < 0.05$ and $R > 1$.

Code availability. Code is available from the corresponding authors upon request.

Statistical analysis. Each statistical test was used according to the design of the experiment and the structure of the data. Two-group comparisons were performed using t-test, Mann–Whitney or Wilcoxon matched-pairs tests depending on the normality of a distribution. Assessment of effects in experiments involving several conditions was performed using ANOVA, followed, when appropriate, by Bonferroni (for pre-selected contrasts) or Tukey tests, adjusting for multiple comparisons. Grubbs' test was used to exclude outlier points from behavioural datasets. Depending on the normality of a distribution, Pearson's or Spearman's correlations were computed. For group comparisons, two-tailed statistical tests were applied. Sample size was determined according to the accepted practice for the applied assays, no statistical methods were used to predetermine sample size. Conditions of the experiments were accounted during design of analysis algorithms, computations were subsequently performed blindly using automatic selection of data from a database. A detailed description of statistical analysis is provided in the statistical section of the Supplementary Information. Descriptive statistics are reported as mean ± s.e.m.

Neuronal preparation and transfection, cultured neurons. Primary cultured neurons were prepared from the hippocampi of P_0 Sprague–Dawley rat pups (Charles River Laboratories), as described previously[49]. CA1 and CA3 hippocampal regions were taken out and digested with 0.4 mg ml^{-1} papain (Worthington), and plated onto 12-mm glass coverslips that were pre-coated with 1:30 Matrigel (Beckton Dickinson Labware).

Cultures were kept under neurobasal-A medium (Invitrogen) containing 1.25% FBS (HyClone), 4% B-27 supplement (Gibco), 2 mM glutamax (Gibco) and 2 mg ml^{-1} fluorodeoxyuridine (FUDR, Sigma) and plated at a density of 65,000 cells per well in 24-well plates. The plates were incubated at 37 °C in a humid incubator with a constant level of 5% CO_2.

Cultured neurons were transfected at 6–10 days *in vitro* (DIV). A DNA–CaCl$_2$ mix composed of the following was prepared for transfection per well: 1 μg of

endotoxin-free DNA for recordings, 1.875 µl 2 M CaCl₂, and sterile H₂O for a total volume of 15 µl. Another 15 µl of twice-filtered HEPES-buffered saline (HBS, in mM: 50 HEPES, 1.5 Na₂HPO₄, 280 NaCl, pH 7.05 with NaOH) for each DNA–CaCl₂ mix. This mix was incubated at room temperature for 20 min. In the meantime, the neuronal growth medium was removed from the wells and kept at 37 °C, and replaced with 400 µl pre-warmed minimal essential medium (MEM). After incubation of the DNA–CaCl₂–HBS mix was complete, the mix was then added dropwise into each well, and plates were incubated for 45–60 min at 37 °C. Once the transfection was complete, each well was washed three times with 1 ml of pre-warmed MEM. The MEM was then replaced with the original neuronal growth medium, and plates were placed into the culture incubator at 37 °C.

In vitro electrophysiology, cultured neurons. Whole-cell patch-clamp recordings of cultured hippocampal neurons were performed 3–5 days after transfection with the construct AAVdj-hSyn-NpHR-TS-p2A-hChR2(H134R)-eYFP (eNPAC2.0). Expression of the construct was identified by eYFP fluorescence. The external recording medium was composed of the following (in mM): 125 NaCl, 2 KCl, 25 HEPES, 2 CaCl₂, 2 MgCl₂, 30 D-(+)-glucose. pH 7.3, with synaptic transmission blockers D-2-amino-5-phosphonovaleric acid (AP5; 25 µM), 2,3-dihydroxy-6-nitro-7-sulfamoyl-benzo[f]quinoxaline-2,3-dione (NBQX; 10 µM), and gabazine (10 µM). The intracellular recording solution contained (in mM): 130 potassium gluconate, 10 KCl, 10 HEPES, 10 EGTA and 2 MgCl₂. An upright microscope (BX61WI, Olympus) with infrared differential interference contrast (IR-DIC) was used for visualization and recording of the expressing neurons. A Spectra X Light engine (Lumencor) attached to the fluorescent port of the microscope was used for light application, for detecting eYFP expression and for blue or yellow light delivery for opsin activation. A 475/28 nm and a 586/20 nm filter (Chroma) were used for blue and yellow light respectively (Chroma). A power meter (ThorLabs) was used to measure the light power through the microscope objective, and light power density was set at 5 mW mm⁻¹ (ref. 49). Recordings were obtained using a MultiClamp700B amplifier, 1440A Digidata digitizer, and pClamp10.3 software (Molecular Devices). Data were analysed with pClamp10.3 and SigmaPlot (SPSS).

Photocurrent amplitudes at blue and yellow were measured at steady-state at the end of a 1-s light stimulation protocol. To measure spike inhibition probability at 586 nm, we first applied a 50–200 pA electrical current injection (depending on spike threshold of the recorded cell) to induce spiking in the expressing neurons. Spike inhibition probability was calculated as the percentage in which yellow light application inhibited spiking during the electrical current injection. To measure spike generation probability with blue light, we applied 5-ms width pulses of 475 nm light at 5 or 20 Hz frequency, and calculated the percentage of action potentials generated by the blue light pulse train. Series resistance was carefully monitored for stability throughout the recordings. To ensure accurate measurements of voltage-clamp recordings, data were incorporated for analysis only if the series resistance was below 25 MΩ and changed less than 20% throughout the recording.

In vitro electrophysiology, LH slices. Standard whole-cell slice patch-clamp recordings were undertaken after slice preparation of at least 2-month-old mice. In brief, after gluing a block of brain with cyanoacrylate glue to the stage of a Campden Vibroslice, coronal brain slices of 250-µm thickness containing the LH were cut while immersed in ice-cold slicing solution. Slices were incubated for 1 h in artificial cerebrospinal fluid (ACSF) at 35 °C then transferred to a submerged-type recording chamber. Living neurons containing fluorescent markers were visualized in acute brain slices with an upright Olympus BX61WI microscope equipped with an oblique condenser and appropriate fluorescence filters. After identifying appropriate neurons by their fluorescence, oscillatory currents of 10 pA amplitude (30, 50, 70 and 100 Hz) were injected for 5 s to the cell during whole-cell patch-clamp recordings. Recordings of membrane potentials were analysed in MatLab.

To record selectively from Vgat neurons, a cross between Vgat-ires-Cre and CAG-tdTomato mice[33] was used. To target MCH-Cre neurons selectively, MCH-Cre mice were injected into the LH (1.3 mm caudal from bregma; ±0.95 mm lateral from midline; and 5.25 and 5.15 mm ventral from brain surface) with a Cre-dependent ChR-mCherry.

For brain slice recordings, ACSF and ice-cold slicing solution were gassed with 95% O₂ and 5% CO₂, and contained the following (in mM) ACSF: 125 NaCl, 2.5 KCl, 1 MgCl₂, 2 CaCl₂, 1.2 NaH₂PO₄, 21 NaHCO₃, 2 D-(+)-glucose, 0.1 Na⁺-pyruvate and 0.4 ascorbic acid. Slicing solution: 2.5 KCl, 1.3 NaH₂PO.H₂0, 26.0 NaHCO₃, 213.3 sucrose, 10.0 D-(+)-glucose, 2.0 MgCl₂ and 2.0 CaCl₂. For standard whole-cell recordings, pipettes were filled with intracellular solution containing the following (in mM): 120 K-gluconate, 10 KCl, 10 HEPES, 0.1 EGTA, 4 K₂ATP, 2 Na₂ATP, 0.3 Na₂GTP and 2 MgCl₂, pH 7.3 with KOH.

Multitaper power spectra of voltage traces and of injected current traces were computed and divided, resulting in impedance spectra. Mean impedance at ±1.5 Hz around stimulation frequency was computed.

CLARITY. Brain hemispheres were clarified using the CLARITY procedure as described elsewhere[27]. In brief, a brain hemisphere was fixed in hydrogel solution (4% PFA, 1% acrylamide/bis) for 72 h at 4 °C. After polymerization (37 °C, 4 h), the brain hemispheres were clarified in 8% SDS for 8 days (at 40 °C), then washed three times with PBST (0.2% Triton X-100) for a total of 24 h at 37 °C.

Light-sheet imaging. Hemisphere images were acquired with the Ultramicroscope II (Lavision Biotec)[27]. Samples were mounted to a custom 3D printed holder using RapidClear Mounting Gel (Sunjin laboratory). Brains were imaged using a 2×/0.5 NA objective at 0.8× zoom using a single light sheet illuminating from the dorsal side of the sample. Z-step was set to 4 µm. Fourteen horizontal focal points were set to each imaging plane to create a homogeneous field of view.

For synapsin staining the brains were cut, after CLARITY processing, into 1-mm-thick sections. Primary antibody: rabbit anti-synapsin (Cell Signaling, 5297), 1:400, in 0.3% PBST, room temperature, 24 h; secondary antibody: donkey anti-rabbit (Alexa 594, Jacksonimmuno), 1:200, in 0.3% PBST, room temperature, 24 h; then sections were refractive index-matched and mounted in RapidClear CLARITY-specific gel (Sunjin Laboratory). Sections were imaged at bregma = 0.5 using Olympus FV1200 confocal, 40×, 1.3 NA, oil objective, at 4× zoom.

For synaptophysin imaging, brains expressing CaMKIIa-synaptophysin-mCherry in the mPFC were cut into 0.5-mm-thick section for CLARITY clearing and imaging. The sections were imaged at bregma = 0.5 using Olympus FV1200 confocal, 40×, 1.3 NA, oil objective, at 4× zoom.

Histology and microscopy. After completion of the experiments, mice were deeply anaesthetized and electrolytic lesions at selected recording sites were performed. Subsequently, the mice were perfused intracardially with saline followed by 4% paraformaldehyde in PBS and decapitated. Brains were fixed overnight in 4% paraformaldehyde, equilibrated in 1% PBS for an additional night and finally cut into 40 or 50 µm slices using an oscillating tissue slicer (EMS 4500, Electron Microscopy Science). Brain slices were mounted (Flouromount Aqueous Mounting Medium, Sigma-Aldrich). Images were taken using an Olympus BX 61 microscope (×2/0.06 NA, ×10/0.3 NA and ×20/0.5 NA, dry) or using a Leica DMI 6000 microscope (×20/0.7 NA, ×63/1.4 NA; oil-immersion objectives).

Data availability. All data generated or analysed during this study are either included in this published article or are available from the corresponding authors on reasonable request.

31. Vong, L. et al. Leptin action on GABAergic neurons prevents obesity and reduces inhibitory tone to POMC neurons. Neuron 71, 142–154 (2011).
32. Taniguchi, H. et al. A resource of Cre driver lines for genetic targeting of GABAergic neurons in cerebral cortex. Neuron 71, 995–1013 (2011).
33. Madisen, L. et al. A robust and high-throughput Cre reporting and characterization system for the whole mouse brain. Nat. Neurosci. 13, 133–140 (2010).
34. Kim, S. Y. et al. Diverging neural pathways assemble a behavioural state from separable features in anxiety. Nature 496, 219–223 (2013).
35. Vandecasteele, M. et al. Large-scale recording of neurons by movable silicon probes in behaving rodents. J. Vis. Exp. 61, e3568 (2012).
36. Jennings, J. H., Rizzi, G., Stamatakis, A. M., Ung, R. L. & Stuber, G. D. The inhibitory circuit architecture of the lateral hypothalamus orchestrates feeding. Science 341, 1517–1521 (2013).
37. Korotkova, T., Fuchs, E. C., Ponomarenko, A., von Engelhardt, J. & Monyer, H. NMDA receptor ablation on parvalbumin-positive interneurons impairs hippocampal synchrony, spatial representations, and working memory. Neuron 68, 557–569 (2010).
38. Hazan, L., Zugaro, M. & Buzsáki, G. Klusters, NeuroScope, NDManager: a free software suite for neurophysiological data processing and visualization. J. Neurosci. Methods 155, 207–216 (2006).
39. Sirota, A. et al. Entrainment of neocortical neurons and gamma oscillations by the hippocampal theta rhythm. Neuron 60, 683–697 (2008).
40. Mitzdorf, U. Current source-density method and application in cat cerebral cortex: investigation of evoked potentials and EEG phenomena. Physiol. Rev. 65, 37–100 (1985).
41. Kajikawa, Y. & Schroeder, C. E. How local is the local field potential? Neuron 72, 847–858 (2011).
42. Harris, K. D., Henze, D. A., Csicsvari, J., Hirase, H. & Buzsáki, G. Accuracy of tetrode spike separation as determined by simultaneous intracellular and extracellular measurements. J. Neurophysiol. 84, 401–414 (2000).
43. Wulff, P. et al. Hippocampal theta rhythm and its coupling with gamma oscillations require fast inhibition onto parvalbumin-positive interneurons. Proc. Natl Acad. Sci. USA 106, 3561–3566 (2009).
44. Siapas, A. G., Lubenov, E. V. & Wilson, M. A. Prefrontal phase locking to hippocampal theta oscillations. Neuron 46, 141–151 (2005).
45. Fidzinski, P. et al. KCNQ5 K⁺ channels control hippocampal synaptic inhibition and fast network oscillations. Nat. Commun. 6, 6254 (2015).
46. Csicsvari, J., Hirase, H., Czurkó, A., Mamiya, A. & Buzsáki, G. Oscillatory coupling of hippocampal pyramidal cells and interneurons in the behaving Rat. J. Neurosci. 19, 274–287 (1999).
47. Zhang, S. J. et al. Optogenetic dissection of entorhinal-hippocampal functional connectivity. Science 340, 1232627 (2013).
48. Muller, R. U. & Kubie, J. L. The firing of hippocampal place cells predicts the future position of freely moving rats. J. Neurosci. 9, 4101–4110 (1989).
49. Berndt, A. et al. Structural foundations of optogenetics: Determinants of channelrhodopsin ion selectivity. Proc. Natl Acad. Sci. USA 113, 822–829 (2016).
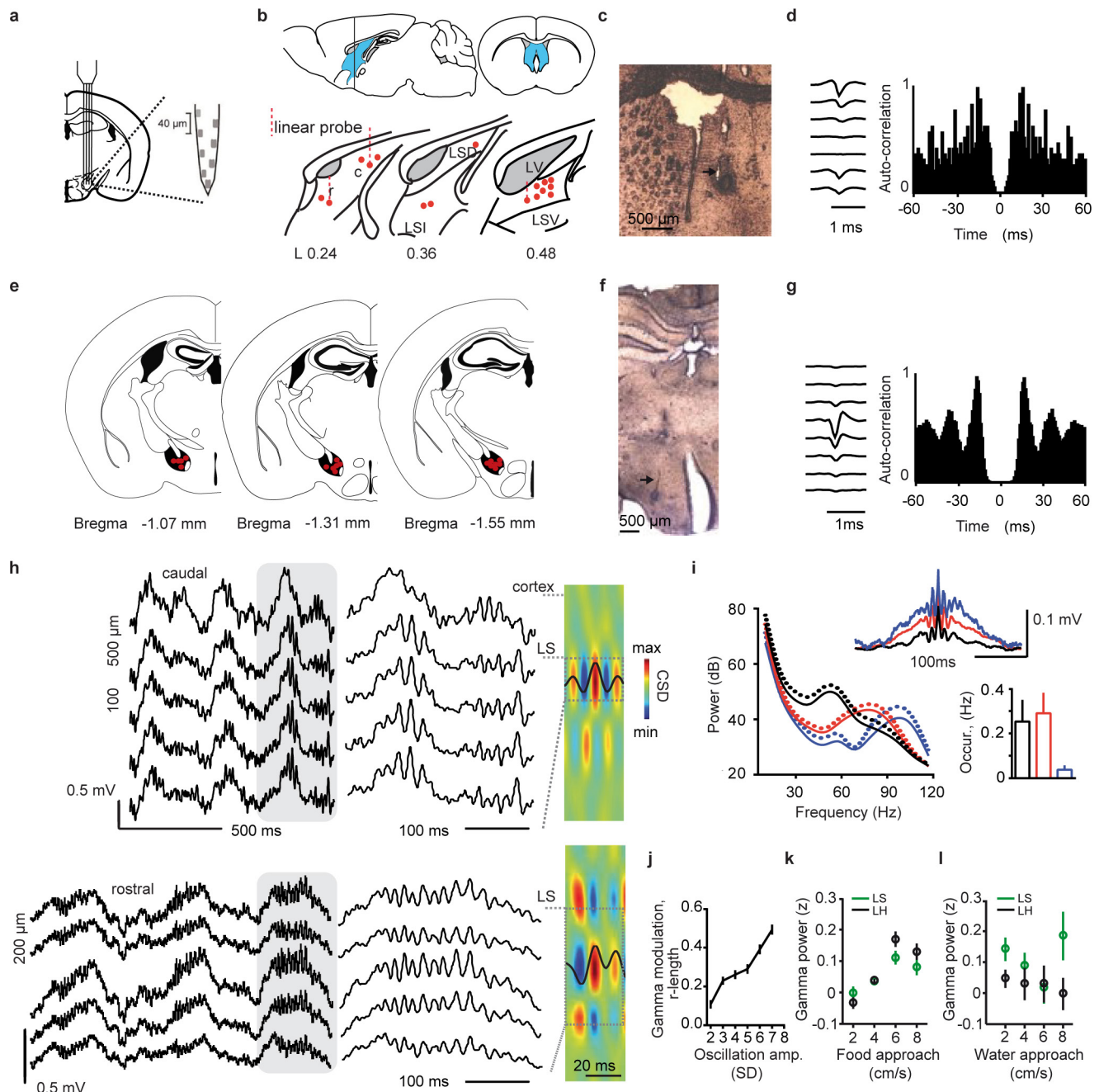
Extended Data Figure 1 | Gamma oscillations in the LS and the LH.
a, Schematic of a B32/B64 silicon probe shank. Inset shows the active area of a probe shank with eight recording sites. **b**, The LS is depicted in blue on sagittal and coronal planes. Bottom, reconstruction of the positions of recording electrodes in the LS; red dots show sites of electrolytic lesions/ electrode tracks in each mouse. Lateral (L) 0.24–0.48 mm, distance to midline. CM32 linear probe recordings from caudal (c) and rostral (r) sites are shown in **h**. LSD, LSI and LSV denote dorsal, intermediate and ventral LS, respectively. **c**, A representative brain section. Arrow indicates localization of an electrolytic lesion in the LS. **d**, An example of an isolated single LS unit. Average spike waveforms (left) recorded using a silicon probe (image shown in **a**), and the corresponding auto-correlogram (right). Bin width, 1 ms. **e**, Reconstruction of recording electrodes positions in the LH; red dots show sites of electrolytic lesions in each mouse. **f**, A representative brain section showing a silicon probe track and a lesion in the LH (arrow). **g**, An example of an isolated single LH unit. Average spike waveforms (left) recorded using a silicon probe (image shown in **a**), and the corresponding auto-correlogram (right). Bin width, 1 ms. Note prominent gamma rhythmicity of the discharge. **h**, Examples of multisite recordings of LFP from caudal (top) and rostral (bottom) LS using linear silicon probes. The top trace in the caudal recording

shows cortical LFP; recording epochs highlighted in grey are expanded. Colour panels: current source density (CSD) maps showing local gamma oscillatory activity in the LS. CSD was computed from the average depth profiles of gamma oscillations in respective recording sessions. Black waveform on each colour panel shows average gamma-band signal in the channel used to detect oscillations. **i**, Left, power spectral density of gamma oscillation episodes, with leading frequencies in one of the three sub-bands: black: 30–60 Hz; red: 60–90 Hz; blue: 90–120 Hz. Right, occurrence of gamma episodes. Top, average 1–200 Hz LFP signal centred at peaks of gamma envelopes with respective leading frequencies. **j**, Rhythmic modulation of neuronal discharge in the LS was higher during gamma oscillations of larger amplitude (30–90 Hz gamma amplitude: $P < 0.00001$, ANOVA, $n = 75$ cells). **k**, Power of LFP gamma oscillations (30–60 Hz) in the LS and LH matched the time required to reach food zone from a given location (approach rate, LS: $n = 79$ experiments, $n = 13$ mice, $P = 0.000023$; LH: $n = 83$ experiments, $n = 16$ mice; $P < 0.00001$, ANOVA). **l**, Power of LFP gamma oscillations (30–60 Hz) in the LS and LH did not match the time required to reach the drinking zone (approach rate, LS: $n = 43$ experiments, $n = 7$ mice, $P = 0.13$; LH: $n = 48$ experiments, $n = 11$ mice, $P = 0.98$, ANOVA). Data are mean ± s.e.m. The mouse brain was reproduced with permission from ref. 30.
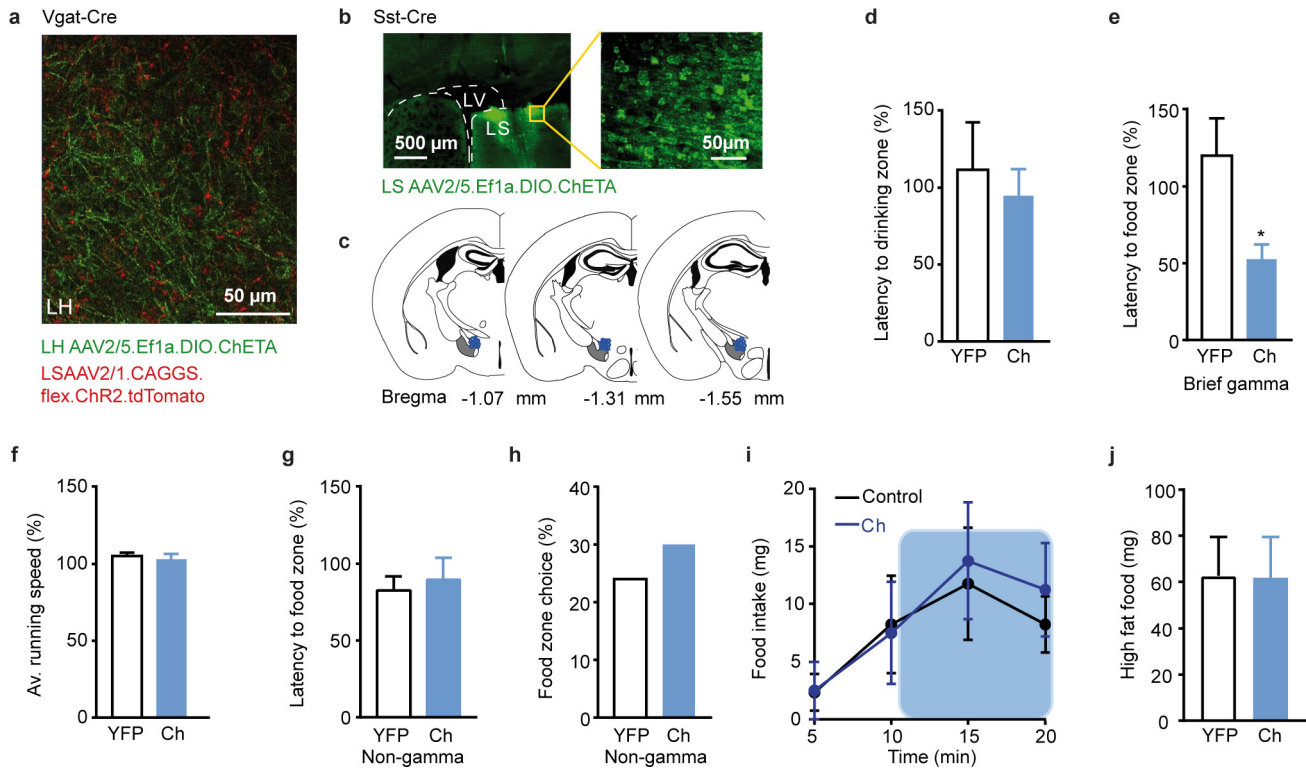
Extended Data Figure 2 | Role of the LS–LH pathway in feeding behaviour. a, Fluorescence image of a coronal LH section showing fibres of ChR2-tdTomato-expressing LS_{Vgat} cells (red), and ChETA–YFP expressing LH_{Vgat} neurons (green). The two constructs were used in the same mouse to visualize LS_{Vgat} projections to the LH. For behavioural experiments, only one brain region was targeted in each mouse. **b**, Expression of Cre-dependent ChETA in the LS in a Sst-Cre mouse. **c**, Reconstruction of termination sites of optic fibres (blue circles) in the LH; ten representative sites for a given bregma position, representing the whole range of termination positions, are shown. **d**, Latency to reach the drinking zone after the onset of LS_{SST}–LH pathway stimulation at gamma frequency (YFP: $n = 6$ mice, opsin: $n = 9$ mice; $P = 0.6$, t-test). **e**, Latency to reach the food zone after the onset of brief (30 s) stimulation of the LS_{SST}–LH pathway at gamma frequency (YFP: $n = 9$ mice, opsin: $n = 11$ mice; *$P = 0.01$ t-test). **f**, LS_{SST}–LH optostimulation with ChETA (Ch) at gamma frequency did not change the average running speed (YFP: $n = 7$ mice,

Ch opsin: $n = 12$ mice; $P = 0.6$, t-test). **g**, Latency to reach the food zone after the onset of LS_{SST}–LH pathway stimulation at non-gamma (theta) frequency (opsin: $n = 7$ mice) compared to intensity-matched stimulation in the YFP group ($n = 8$ mice; $P = 0.7$, t-test). **h**, LS_{SST}–LH optostimulation at non-gamma (theta) frequency did not change the fraction of trials in which a mouse visited the food zone before the other three corners of the enclosure (opsin: $n = 8$ mice, YFP, intensity-matched stimulation: $n = 8$ mice; $P = 0.5$, binomial test). **i**, Amount of food consumed during control stimulation (black) or optogenetic stimulation (blue) of LS_{SST}–LH projections at gamma frequency performed in the same mice ($n = 6$ mice; $P = 0.13$ ANOVA). **j**, Amount of high-fat food (60% energy from fat) consumed per 10 min after LS_{SST}–LH pathway stimulation at gamma frequency (YFP: $n = 7$ mice, opsin: $n = 6$ mice; $P = 0.97$. t-test). Data are mean ± s.e.m. The mouse brain was reproduced with permission from ref. 30.
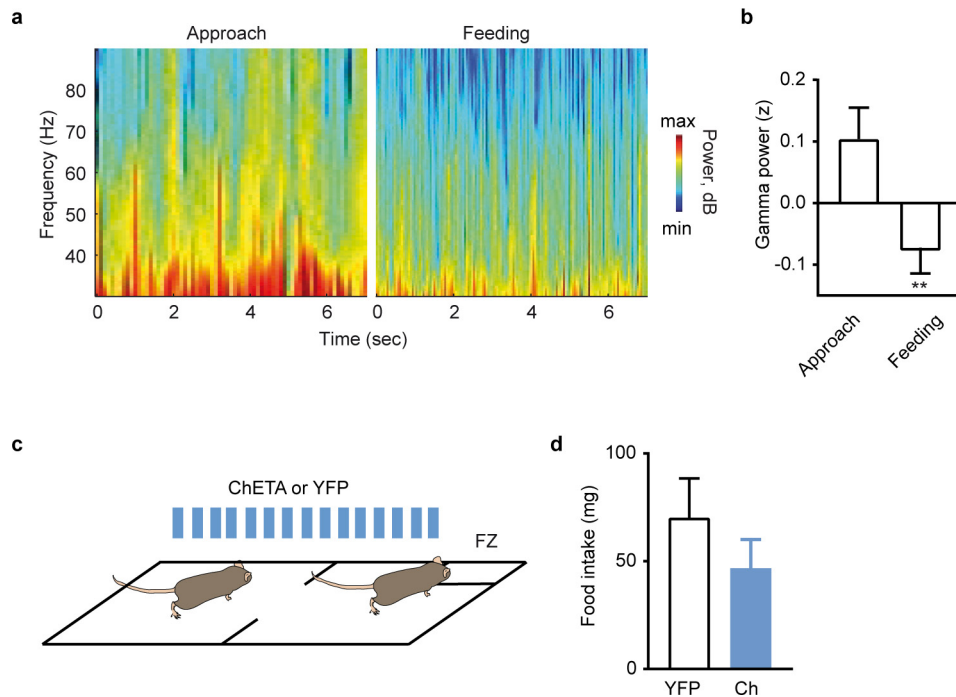
Extended Data Figure 3 | Gamma oscillations during feeding.
a, Representative spectrograms (30–90 Hz band) computed from the LH LFP during the food approach and feeding in the same recording session, power is scaled from minimum to maximum across the two plots. **b**, Power of LFP gamma oscillations (30–90 Hz) in the LH during food approach and feeding ($n = 3$ mice; **$P = 0.0088$, ANOVA). **c**, **d**, When LS_{SST}–LH gamma-rhythmic optogenetic stimulation was limited to the area outside the food zone (**c**), no changes in food intake were observed in ChETA-expressing mice compared to YFP-expressing mice (**d**, YFP: $n = 6$ mice, Ch opsin: $n = 6$ mice; $P = 0.33$, t-test). Data are mean ± s.e.m.
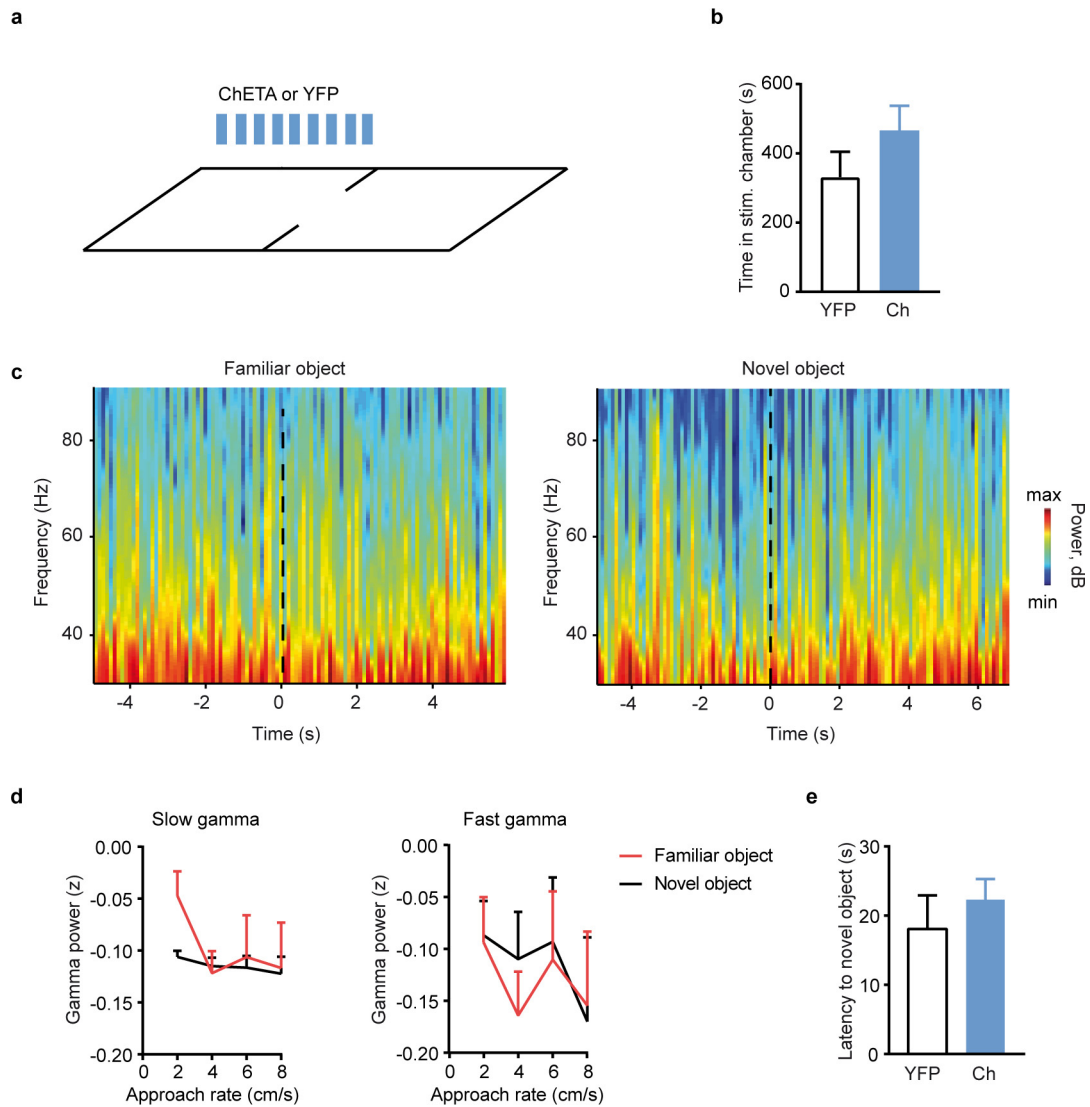
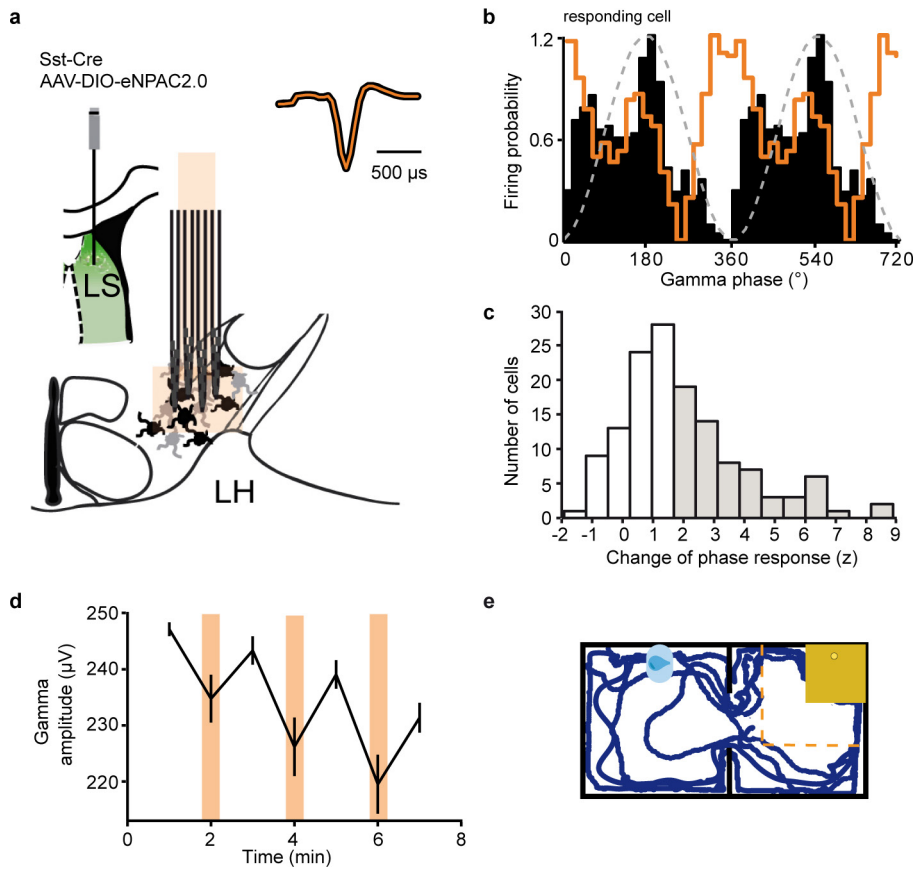**Extended Data Figure 4 | Gamma oscillations and non-food salience.**
a, **b**, Optogenetic activation of excitatory opsin-expressing LS_{SST}–LH projections did not change the time spent in the photostimulation-paired side in a place-preference test compared with YFP-expressing controls (YFP: $n = 7$ mice, opsin: $n = 7$ mice; $P = 0.2$, t-test). **c**, Representative spectrograms (30–90 Hz) computed from the LH LFP during approach to a familiar or a novel object. Dotted line marks the beginning of a contact with the object. **d**, Left, power of 30–60 Hz gamma oscillations during approach to a familiar object (factor 'approach rate', $P = 0.7$, ANOVA) and to a novel object ($P = 0.63$, ANOVA). Right, power of 60–90 Hz gamma oscillations during approach to a familiar object ($P = 0.7$, ANOVA) and a novel object ($n = 3$ mice; $P = 0.07$, ANOVA). **e**, Gamma-rhythmic optogenetic stimulation of the LS_{SST}–LH pathway did not change latency to reach a novel object (YFP: $n = 5$ mice, opsin: $n = 8$ mice; $P = 0.45$, t-test). Data are mean $\pm$ s.e.m.
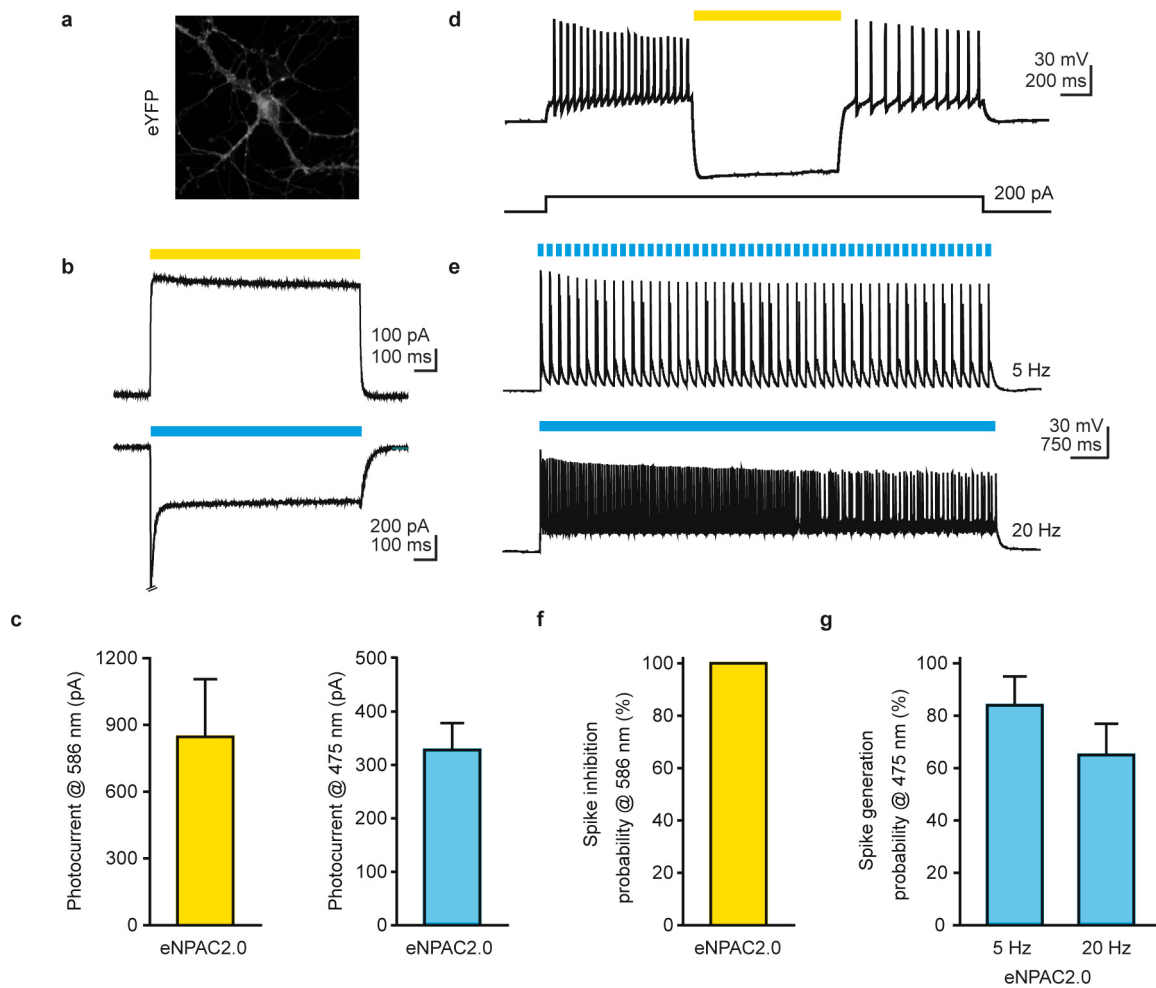
Extended Data Figure 5 | Opposing control of neuronal excitability in the same cell with the eNPAC2.0 construct. a, Sample image of an eNPAC2.0-expressing neuron under eYFP fluorescence. **b**, Example voltage-clamp recordings from an eNPAC2.0-expressing neuron after yellow (586/20 nm, top trace) and blue (475/28 nm, bottom trace) light delivery. Escape spike within peak inward current is truncated for clarity. **c**, Bar graph summaries of steady-state photocurrent amplitudes after yellow and blue light application. **d**, Example current-clamp recording showing yellow-light-mediated inhibition of electrically induced spiking in an eNPAC2.0-expressing neuron (200 pA electrical current injection). **e**, Example current-clamp recordings showing blue-light-induced spiking in the same neuron. Blue light pulse widths were 5 ms, delivered at 5 Hz (top trace) or 20 Hz (bottom trace). **f**, Bar graph summary of spike inhibition probability during delivery of yellow light. **g**, Spike generation probability under 5 Hz and 20 Hz blue-light pulse trains. Light power density: 5 mW mm^{-2} for yellow and blue light. $n = 9$ cells. Data are mean ± s.e.m.

a

Sst-Cre
AAV-DIO-eNPAC2.0

500 μs

LS

LH

b

responding cell

Firing probability

Gamma phase (°)

c

Number of cells

Change of phase response (z)

d

Gamma amplitude (μV)

Time (min)

e

Extended Data Figure 6 | LS$_{SST}$–LH inhibition in behaving mice using eNPAC2.0. a, Optogenetic inhibition of LS$_{SST}$–LH projections in eNPAC2.0-expressing Sst-Cre mice. **b**, Average spike waveforms and firing probability during gamma cycle of a representative LH cell, responding to LS$_{SST}$–LH inhibition, before (black) and during (orange) 593 nm light delivery onto LS$_{SST}$–LH projections. **c**, Changes of gamma phase response in LH cells after LS$_{SST}$–LH inhibition ($n = 138$ cells). Grey bars denote significantly ($P < 0.05$) responding cells (see Supplementary Information, Statistical Analysis). **d**, LH gamma amplitude changes after LS$_{SST}$–LH optogenetic inhibition; orange rectangles show 1-min epochs when the yellow light was delivered. **e**, Yellow light was delivered onto eNPAC2.0-expressing LS$_{SST}$–LH projections as mice entered the food approach zone (orange dotted line). Data are mean ± s.e.m. The mouse brain was reproduced with permission from ref. 30.
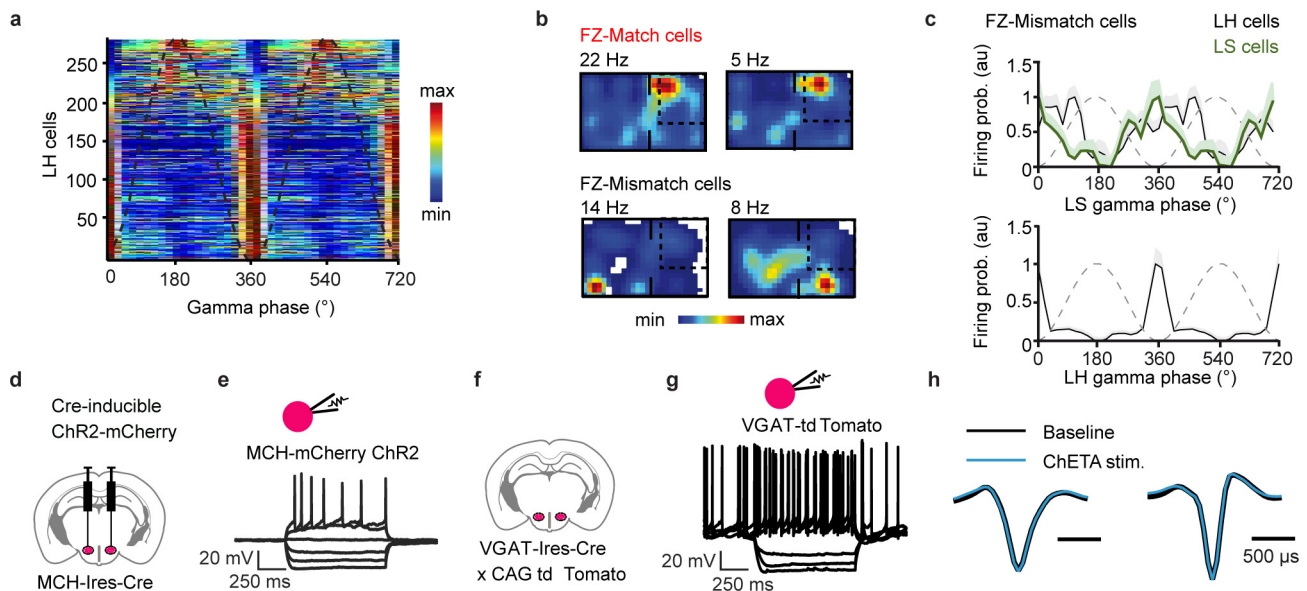
Extended Data Figure 7 | Firing of functionally and genetically identified LH neurons *in vivo* and *in vitro*. a, Firing of individual LH cells during locally recorded slow gamma oscillations (30–60 Hz, $n = 291$ cells). Colour scale indicates normalized for each neuron firing probability. **b**, Example firing maps of LH cells that fire preferentially in the food zone (top, FZ-match cells) and outside the food zone (bottom, FZ-mismatch cells). Maximal firing rate of each cell is shown above the colour maps. **c**, Changes in firing probability of LH FZ-mismatch cells during spontaneous LS (top) and LH (bottom) gamma oscillations (30–60 Hz, $n = 55$ cells). Firing probability of LS cells according to phase

of LS gamma oscillation ($n = 69$ cells). **d**, To identify MCH cells, MCH-Cre mice were injected into the LH with a Cre-dependent ChR2-mCherry virus. **e**, Voltage responses of an identified MCH cell to current pulses (-60, -40, -20, 0, $+20$, $+40$ pA). **f**, To identify Vgat-expressing cells, a cross between Vgat-ires-Cre and CAG-tdTomato mice was used. **g**, Voltage responses of an identified Vgat-expressing LH cell to current pulses (-60, -40, -20, 0, $+20$, $+40$ pA). **h**, Average spike waveforms of representative presumed LH Vgat cells before (black) and during (blue) LH$_{Vgat}$ optostimulation. Data are mean ± s.e.m. The mouse brain was reproduced with permission from ref. 30.
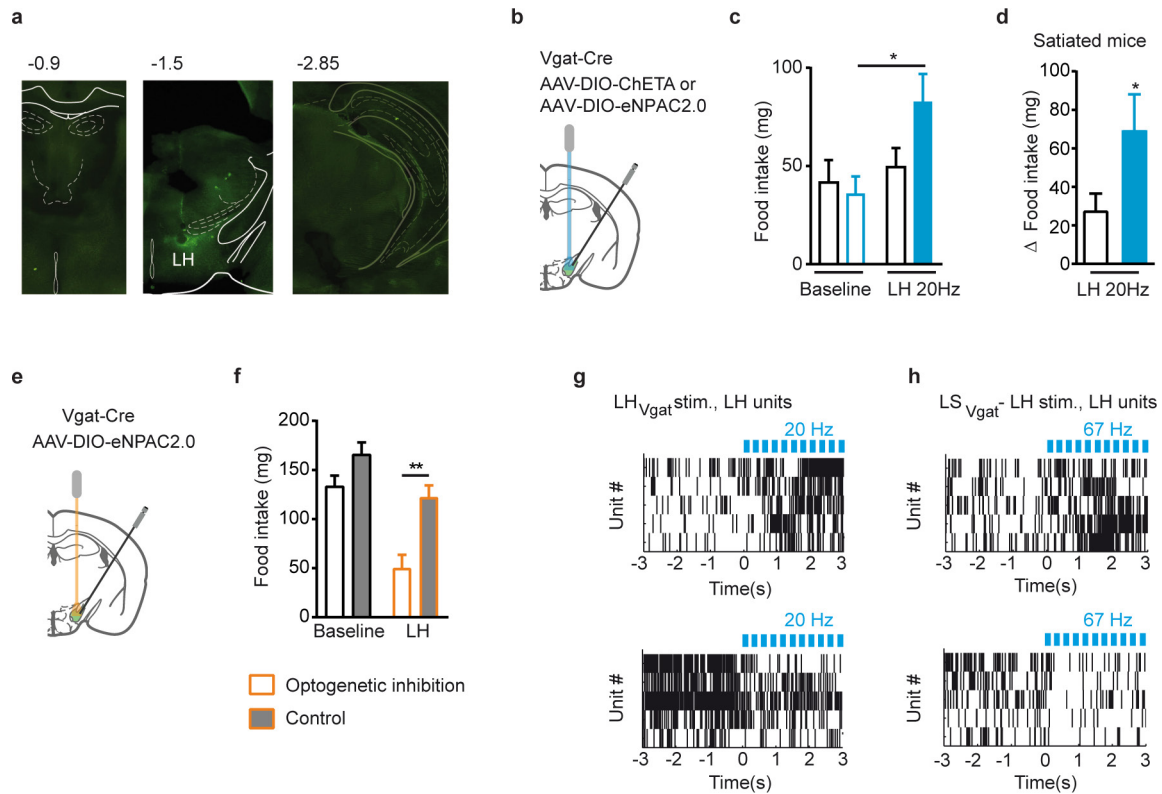
Extended Data Figure 8 | Opposing optogenetic control of LH$_{Vgat}$ cells bidirectionally manipulates food intake. a, Photomicrographs showing anterior-posterior coronal brain sections from Vgat-Cre mice transduced with AAV-ChETA-eYFP in the LH area. **b**, For optostimulation of LH$_{Vgat}$ cells, Cre-dependent opsins ChETA or eNPAC2.0 were expressed in Vgat-ires-Cre mice, and blue light (473 nm) was delivered at 20 Hz to the LH. **c, d**, Optostimulation of LH$_{Vgat}$ cells increased food intake (**c**, optogenetic stimulation: $n = 5$ mice, control stimulation: $n = 7$ mice, *$P = 0.0078$ (LH 20 Hz versus baseline), $P = 0.23$ (control stimulation versus control baseline), ANOVA; also in a subset of experiments (**d**) in which the mice were satiated (consumed <3 pellets during the baseline recording; optogenetic stimulation: $n = 5$ mice; control: $n = 6$ mice; *$P = 0.0016$, ANOVA). **e**, For optogenetic inhibition of LH$_{Vgat}$ cells,

yellow light (593 nm) was bilaterally delivered into the LH in Vgat-ires-Cre mice, expressing Cre-dependent opsin (eNPAC2.0). **f**, Optogenetic inhibition of the LH$_{Vgat}$ cells decreased food intake in food-deprived mice (LH: $n = 12$ experiments, $n = 3$ mice; baseline: $n = 12$ experiments, $n = 3$ mice; yellow-light stimulation (orange open bar) decreased amount of pellets eaten compared to control stimulation (orange filled bar), **$P = 0.0003$, ANOVA, Tukey tests). **g**, Examples of fast (within 3 s) discharge changes in different LH cells during optostimulation of Vgat cells at 20 Hz. **h**, Examples of fast (within 3 s) discharge changes in different LH cells during optostimulation of LS$_{Vgat}$ cells at gamma frequency. Data are mean ± s.e.m. The mouse brain was reproduced with permission from ref. 30.
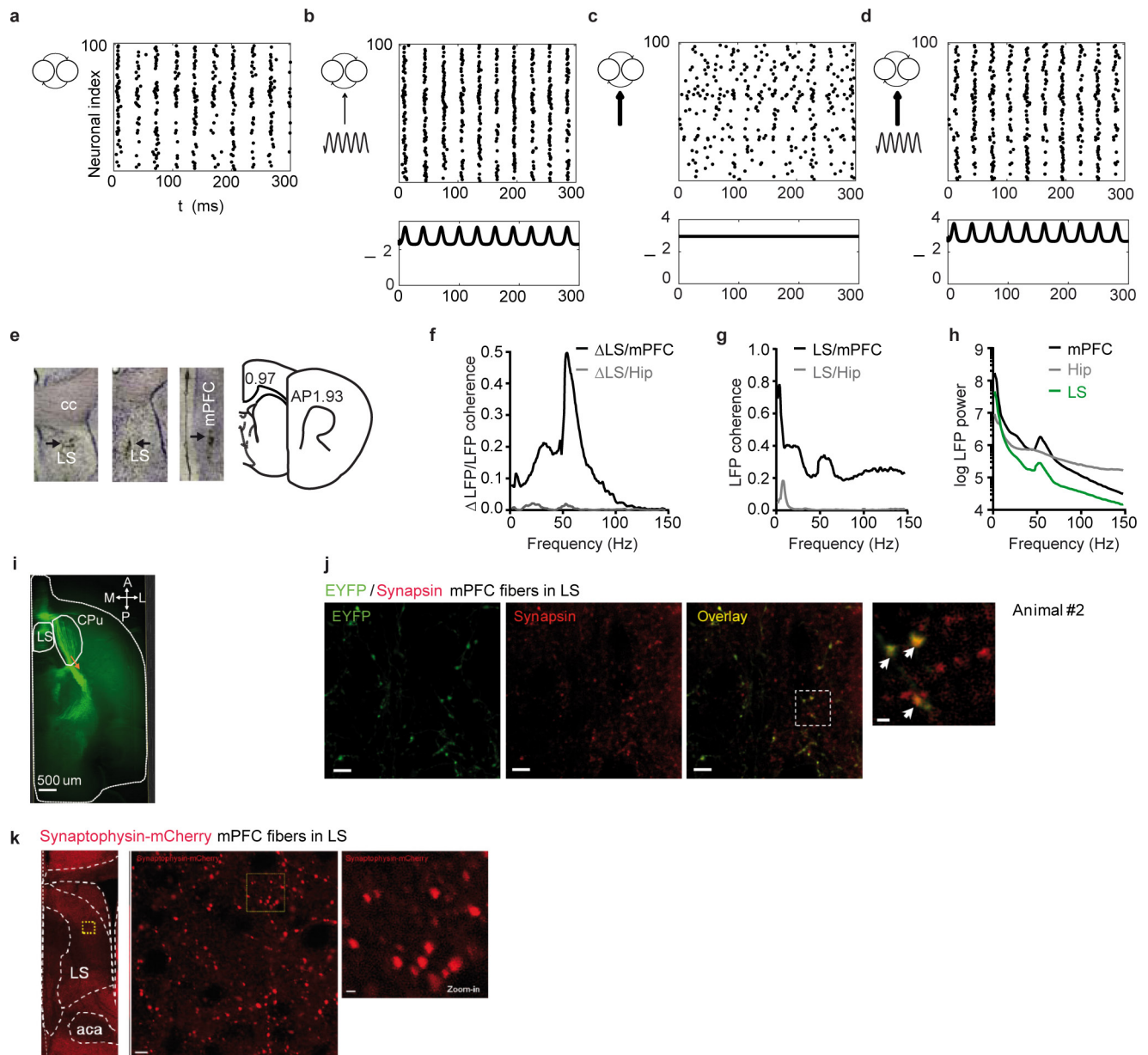
Extended Data Figure 9 | Coordination of gamma oscillations between the LS and mPFC. a–d, Computational modelling of gamma-rhythmic entrainment in the LS. Model network diagrams (left): synaptic connections between inhibitory cells in the LS and inputs to the network, spike rastergrams of 100 cells (top, right) and input current (arbitrary units) to the network (**b–d**, bottom, right). **a**, A deterministic interneuronal network gamma (ING) rhythm with the average cell firing frequency of approximately 12 Hz and a population frequency of 30 Hz. **b**, An external weak gamma-rhythmic input to the network raises average firing rates to around 17 Hz and increases temporal precision of the discharge. **c**, An increase in drive heterogeneity from 2% (**a**) to 20% (**c**) abolishes gamma oscillation. **d**, A weak gamma-rhythmicity of the input in **c** recovers gamma oscillation. **e**, Representative Nissl-stained slices. Arrows highlight electrolytic lesions indicating the locations of probe shanks in the LS and mPFC, at anterior-posterior levels shown on the scheme (right). **f–h**, mPFC–LS and hippocampus–LS LFP coherence spectra (current flow density in the LS, LFP in mPFC or hippocampus, **f**), raw LFP coherence (**g**) and LFP power spectral density (**h**), computed for the recording session, excerpt traces of which are shown in Fig. 4a. A notch at 50 Hz corresponds to the omitted part of the spectrum at mains electricity frequency. **i**, An example image (horizontal view) showing eYFP expression in the projections of mPFC neurons. Images are shown as maximum projection over a 100-µm volume, digitally sliced from the 3D volume shown in Fig. 4c. Note that posterior to the LS, in contrast to caudate putamen, no fibres of passage are seen. **j**, Representative images of eYFP-expressing mPFC fibres in the LS, counterstained with anti-synapsin antibody (1 out of 3 mice). Scale bars, 5 µm (first three images) and 1 µm (right image, which is a magnification of the dotted-line area). An example from a different mouse is shown in Fig. 4e. **k**, Representative images of synaptophysin-mCherry-expressing mPFC fibres in the LS (1 out of 3 mice). Scale bars, 5 µm (middle) and 1 µm (right). The mouse brain was reproduced with permission from ref. 30.
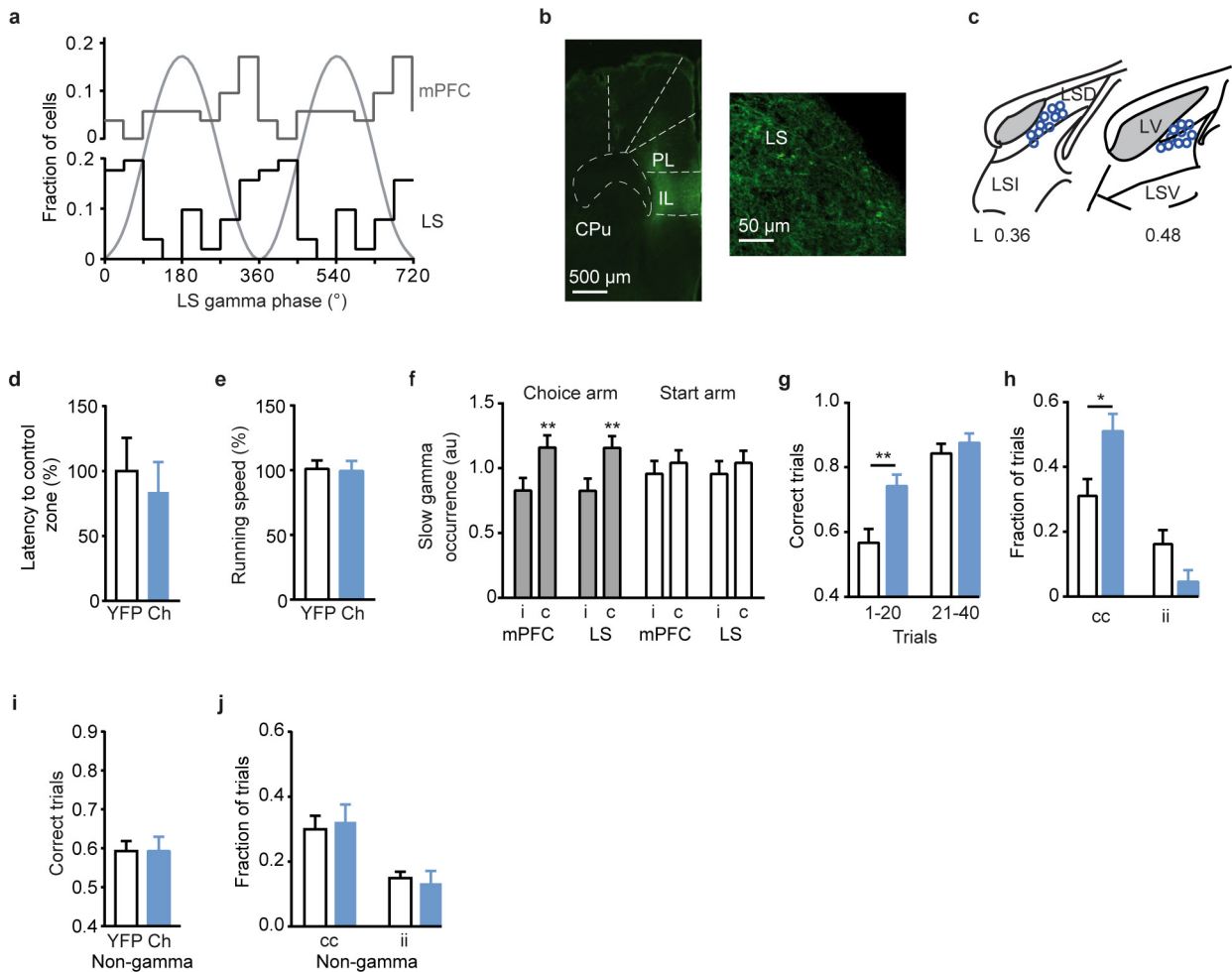
Extended Data Figure 10 | Gamma-rhythmic mPFC–LS signalling improves performance in a T-maze. a, Gamma-rhythmic coordination between firing in the LS and mPFC. LS gamma phase preference of individual slow-firing mPFC cells, that is, a population also including pyramidal cells (<6 Hz, $n = 59$; $P < 0.0001$, Rayleigh test) and LS cells ($n = 73$, $P < 0.0001$, Rayleigh test). Sine waves indicate reference oscillation cycles. Maximal discharge of LS cells followed mPFC neurons by approximately 87° (difference of mean discharge phases: $P < 0.05$, Mardia–Watson test). **b**, Expression of CaMKIIa-dependent ChR2 (AAV2-CaMKIIa-hChR2(H134R)-eYFP) in the somata of mPFC cells (left) and their fibres in the LS (right). IL, infralimbic cortex; PL, prelimbic cortex. **c**, Reconstruction of the termination sites of optic fibres (blue circles) in the LS. Ten representative sites for a given bregma position, representing the whole range of termination positions, are shown. **d**, mPFC–LS stimulation at gamma frequency did not affect the latency to enter the control zone (YFP: $n = 8$ mice, opsin: $n = 7$ mice; $P = 0.7$, t-test). **e**, mPFC–LS stimulation at gamma frequency did not change the average running speed (YFP: $n = 8$ mice, opsin: $n = 7$ mice; $P = 0.7$, t-test). **f**, The occurrence of spontaneous slow (30–60 Hz) gamma oscillation episodes

in the choice segment of the T-maze was increased in correct trials (c) compared to incorrect trials (i) (mPFC: $P = 0.004$, LS: **$P = 0.004$. ANOVA), but was not increased in the start arm of T-maze ($P = 0.4$, ANOVA). $n = 54$ trials, $n = 4$ mice. **g**, The number of correct choices in the T-maze task was increased during mPFC–LS optogenetic stimulation at gamma frequency in water-restricted, water-rewarded mice (YFP: $n = 6$ mice, opsin: $n = 6$ mice, trials 1–20: **$P = 0.0097$, t-test; trials 21–40: $P = 0.4$). **h**, mPFC–LS stimulation at gamma frequency significantly increased the fraction of repeated correct trials (cc) (*$P = 0.02$ t-test), but did not significantly decrease the fraction of repeated incorrect trials (YFP: $n = 6$ mice, opsin: $n = 6$ mice, $P = 0.052$, t-test) in water-restricted, water-rewarded mice. **i, j**, mPFC–LS optostimulation at theta frequency did not change the fraction of correct trials (**i**, trials 1–20, opsin: $n = 7$ mice, YFP, intensity-matched stimulation (same control group as in Fig. 4r, s): $n = 7$ mice, $P > 0.99$, t-test), repeated correct trials (**j**, cc, $P = 0.74$, t-test), or repeated incorrect trials (**j**, ii, $P = 0.7$, t-test). Data are mean ± s.e.m. The mouse brain was reproduced with permission from ref. 30.